

Experimental Investigation of Short Scalelength Density Fluctuations in Laser-Produced Plasmas

*J. D. Moody, B. J. MacGowan, S. H. Glenzer, R. K.
Kirkwood, W. L. Kruer, D. S. Montgomery, A. J. Schmitt,
E. A. Williams, and G. F. Stone*

This article was submitted to
41st Annual Meeting of the Division of Plasma Physics, Seattle, WA, November
15-19, 1999

U.S. Department of Energy

Lawrence
Livermore
National
Laboratory

January 5, 2000

DISCLAIMER

This document was prepared as an account of work sponsored by an agency of the United States Government. Neither the United States Government nor the University of California nor any of their employees, makes any warranty, express or implied, or assumes any legal liability or responsibility for the accuracy, completeness, or usefulness of any information, apparatus, product, or process disclosed, or represents that its use would not infringe privately owned rights. Reference herein to any specific commercial product, process, or service by trade name, trademark, manufacturer, or otherwise, does not necessarily constitute or imply its endorsement, recommendation, or favoring by the United States Government or the University of California. The views and opinions of authors expressed herein do not necessarily state or reflect those of the United States Government or the University of California, and shall not be used for advertising or product endorsement purposes.

This is a preprint of a paper intended for publication in a journal or proceedings. Since changes may be made before publication, this preprint is made available with the understanding that it will not be cited or reproduced without the permission of the author.

This report has been reproduced
directly from the best available copy.

Available to DOE and DOE contractors from the
Office of Scientific and Technical Information
P.O. Box 62, Oak Ridge, TN 37831
Prices available from (423) 576-8401
<http://apollo.osti.gov/bridge/>

Available to the public from the
National Technical Information Service
U.S. Department of Commerce
5285 Port Royal Rd.,
Springfield, VA 22161
<http://www.ntis.gov/>

OR

Lawrence Livermore National Laboratory
Technical Information Department's Digital Library
<http://www.llnl.gov/tid/Library.html>

**Experimental investigation of short scalelength density
fluctuations in laser-produced plasmas**

J. D. Moody, B. J. MacGowan, S. H. Glenzer, R. K. Kirkwood,
W. L. Kruer, D. S. Montgomery¹, A. J. Schmitt², E. A. Williams, and G. F. Stone

Lawrence Livermore National Laboratory

University of California

Livermore, CA 94550

and

¹*Los Alamos National Laboratory*

Los Alamos, NM

and

²*Naval Research Laboratory*

Washington, DC

Abstract

The technique of near forward laser scattering is used to infer characteristics of intrinsic and controlled density fluctuations in laser-produced plasmas. Intrinsic fluctuations are studied in long-scalelength plasmas where we find that the fluctuations exhibit scalesizes related to the intensity variation scales in the plasma-forming and interaction beams. Stimulated Brillouin forward scattering and filamentation appear to be the primary mechanism through which these fluctuations originate. The beam spray resulting from these fluctuations is important to understand since it can affect symmetry in an inertial confinement fusion (ICF) experiment. Controlled fluctuations are studied in foam and exploding foil targets. Forward scattered light from foam targets shows evidence that the initial target inhomogeneities remain after the target is laser heated. Forward scattered light from an exploding foil plasma shows that a regular intensity pattern can be used to produce a spatially correlated density fluctuation pattern. These results provide data which are being used to benchmark numerical models of beam spray.

I. Introduction

Part of achieving a complete physical description of laser-produced plasmas is understanding the role of low frequency density fluctuations. These fluctuations in a laser-plasma set the starting noise level for growth of instabilities such as stimulated Brillouin scattering (SBS) and filamentation. The growth of these instabilities beyond the noise level to saturation may be further affected by fluctuations[1-3]. Low frequency fluctuations also affect laser propagation[4]. For example, experiments show that the laser light can undergo beam spray and increase its bandwidth as a result of active or passive scattering from fluctuations. Fluctuations may arise from the initial structure of the target material, such as in the case of a foam, or may be imposed on the target plasma by the ponderomotive/thermal pressure arising from the intensity structure within the laser beams. A comprehensive description of a laser-plasma includes quantification of the fluctuations and an understanding of how the fluctuations affect the laser-plasma interactions and laser propagation.

In addition to the basic physics aspects of fluctuations, their study is important for inertial confinement fusion (ICF)[5-8]. The current schemes for ICF ignition require a highly symmetric illumination of the fuel capsule by x-rays (indirect drive) or laser light (direct drive). A concern for ICF is that fluctuations or laser-plasma instabilities will increase the angular spread (beam spray) of a beam which can cause illumination asymmetry[9] and substantially reduce the yield of an ICF target. Detailed measurements of forward scattered light in ignition relevant plasmas provide an experimental data-base for evaluating the severity of and the physical processes involved in beam spray. Forward scattered light experiments also help identify methods for reducing and controlling the beam spray and testing the codes which model forward scattering.

In the present investigation we have conducted a series of experiments which use the technique of forward scattered light to investigate the character of intrinsic and controlled fluctuations. The distinction between these two types of fluctuations

has to do with the process by which the fluctuations are induced. Intrinsic fluctuations are not created intentionally (as are controlled fluctuations) but arise from the complex interaction between the hydrodynamic evolution of the electron and ion densities and the ponderomotive/thermal pressure from the incident laser beams. Experiments studying intrinsic fluctuations were done in a long scale-length plasma. The aim of these experiments is to determine the beam-spray and fluctuations which are characteristic of a plasma having a similar scale-length and density as the plasma in the beam-heated region of a National Ignition Facility (NIF) hohlraum while illuminated with a laser beam having similar intensity, f/number, and beam smoothing as a NIF laser beam. Forward scattered light measurements show small-angle and large-angle beam spray. Interpretation of these measurements indicates that the small-angle beam spray arises from density inhomogeneities produced by intensity structure in the plasma forming beams. The large angle spray is associated with the higher intensity probe beam used to study backward and forward scattering. The forward scattered light frequency spectrum shows that classical or strongly driven Brillouin forward scattering is the primary mechanism for generating the density fluctuations related to the presence of the high intensity probe laser. Experiments studying controlled fluctuations were done using foam and exploding foil targets. The foam targets showed that the initial foam structure persists in the resulting plasma. These experiments demonstrate that it is possible to control plasma fluctuations with the initial target design. Controlled fluctuations created with a periodic intensity pattern are studied using exploding foil targets. Forward scattered light shows that the periodic intensity pattern impresses a correlated density perturbation on the plasma.

Modeling of the experiments is done with a wave kinetic equation which describes the propagation of laser light through a turbulent plasma. The kinetic equation is used to infer a fluctuation spectrum which describes the results in each experiment. The goal of the modeling is not to calculate the fluctuation spectrum from first principles but to determine the features of the spectrum which are

required to explain the measurements. The large scale-length and exploding foil plasma cases show that the fluctuation spectrum has characteristic length scales which correspond to the scale-lengths of the transverse intensity variations in the lasers incident on the plasma. The foam case shows a fluctuation spectrum with length scales similar to the foam cell size.

The remainder of this paper is divided into four sections. We describe the experiments which investigate intrinsic fluctuations in the next section, Section II. Section III describes experiments with controlled fluctuations. Section IV discusses the wave kinetic model used to describe the measurements. Finally, Section V presents the conclusions.

II. Intrinsic fluctuations

When neither the target nor the laser intensity structure are chosen with fluctuation control as the primary goal we refer to the resulting fluctuations as intrinsic. Our experimental study of intrinsic fluctuations was carried out using gasbag targets to produce a long scalelength plasma. This plasma has similar scalelength and density as a NIF hohlraum plasma and is used primarily to investigate backscattering from a NIF-like laser with f/8 focusing optics.

A. Experimental facility and instruments

1. The Nova laser

The long scalelength plasma experiments were conducted at the Lawrence Livermore National Laboratory using the Nova laser. This is a Nd:glass laser which operates at 1053 nm wavelength. The 10 Nova beams are positioned around a spherical target chamber. The beams are divided into two sets of five which irradiate each side of the target in an even distribution around a 50° cone. The target is illuminated by 351-nm laser light that has been frequency converted from 1053-nm light. Unconverted 1053 and 527-nm light is blocked from striking the target but is

present as stray light in the chamber. Each beam can produce up to about 3 kJ of 351-nm light in a 1 ns constant power pulse.

2. Gasbag target

The long scale-length plasma was made using a gasbag target[10, 11]. This target consists of two circular polyimide membranes attached to the edges of an aluminum washer. The region between the membranes is filled with a hydrocarbon gas to about 1 atm causing the membranes to expand outward in the shape of a balloon. The fill gases consist of various CH mixtures. The resulting plasma density is varied between about 7.5% and 15% of critical density for 351-nm light by changing the gas type and fill pressure. An argon dopant of 1% is added for x-ray spectroscopic measurements of electron temperature.

Gasbag plasmas have been extensively characterized with both experimental measurement and hydrodynamic simulation[12-15]. Gated x-ray pinhole camera measurements show that the gasbag becomes heated uniformly after about 0.3 to 0.4 ns. The heater beams burn to the target center in about 0.3 ns and create a fairly uniform temperature plasma by 0.4 ns. The rapid blowdown of the gasbag polyimide ‘skin’ when the heater beams initially turn on launches a weak shock which propagates toward the center of the target leaving a rarefaction wave behind. Thomson scattering measurements show that the macroscopic plasma flow is small (about 4×10^6 cm/s) in the central region of the target but steadily increases outside the rarefaction wave. Helium- α and Lyman- α plus dielectronic satellite spectra as well as isoelectronic ratios obtained from x-ray spectroscopic measurements are used to determine the temporal evolution of the electron temperature[14]. These measurements show that the central temperature gradually rises during the time that the heater beams are on to a peak of 2.5 to 3.0 keV. Once the heaters turn off the temperature decreases as the plasma radiates and expands.

Nine of the Nova beams are used to heat the gasbag target and the tenth beam is used as a probe to study forward and backward scattered light. The gasbag laser

setup is shown in Fig. 1 (a). The majority of the gasbag experiments described here used an $f/8.5$ focus lens on the probe beam in order to simulate the laser characteristics from a 4-beamlet quad of NIF. This beam always passes through a kinoform phase plate (KPP)[16] located just after the final focus lens. The KPP spatially smoothes the intensity distribution in the focal spot producing a series of speckles in the laser far-field; the speckles have a width of $3\mu\text{m}$ ($\sim f\lambda$) and a length of about $200\mu\text{m}$ ($8f^2\lambda$). The KPP also produces a nearly flat-top envelope to the laser intensity distribution at focus with an elliptical spot size of $260 \times 400 \mu\text{m}^2$. Two other laser smoothing techniques were implemented by conditioning the laser light prior to passing through the KPP. These techniques are called smoothing by spectral dispersion (SSD)[17-18] and polarization smoothing (PS)[19-22]. SSD was done by applying a 17 GHz oscillating RF field to an electro-optic crystal to modulate the phase of the seed laser pulse. The frequency-broadened pulse was dispersed with a diffraction grating, amplified by the Nova laser amplifiers, and then focused onto the target. The resulting focal spot consists of many speckle patterns which interfere in time and space. The applied FM bandwidth causes the speckle pattern to decorrelate in about 5 ps. Polarization smoothing was done by inserting a 2 by 2 array of birefringent glass between the conversion crystals and the final focus lens. This array was aligned so that the incident laser electric field vector was 45° to both the ordinary and extraordinary axes of the birefringent glass. The glass is slightly wedged so that half of the energy in the incident beam produced a speckle pattern spatially shifted and orthogonally polarized to the speckle pattern formed from the other half of the energy. The smoothing effect from PS is instantaneous whereas the smoothing from SSD requires a decorrelation time for the speckle pattern to change significantly. The pulse-shape of the probe and heater beams is typically trapezoidal with about a 150 ps linear rise and fall and approximately constant power in between (typical variation is 15%). Addition of SSD increases the rise and fall time of the pulse to about 250 ps.

3. Transmitted light measurements

The primary forward scattered light instrument for the Nova experiments consisted of a combined low and high-sensitivity detector[23,24]. Other methods of forward scattered light detection using film have been employed in other experiments described in Refs. [25-27]. A low-sensitivity scatter plate was used to measure the majority of the transmitted light on Nova. The plate had a central section measuring 45 cm in diameter and was surrounded by a scatter-plate annulus extending the overall angular coverage of the scatter plate to about 15° from direct forward. The plate was composed of SiO_2 that was roughened so as to give a uniform scattering surface.

The transmitted light that strikes the main scatter plate is measured using a fast photodiode and a gated optical imager (GOI). The photodiode is bandpass filtered from 345 to 355-nm and has a rise time of 60 ps. Light scattered from the plate arrives at the photodiode over a spread of times because the plate is flat and is viewed at an angle. The photodiode signal is recorded by a scope giving an overall time response of about 250 ps. Deconvolving the plate response function from the diode signal using the light distribution on the plate improves the diode signal time response to about 150 ps.

The GOI takes three images of the 2-D light distribution on the scatter plate with a dynamic range of about 50:1. The gating time for an image is 200 ps and the images are taken at 300, 600, and 900 ps after the probe beam turns on. The images have a resolution at the scatter plate of about 1 cm. Bandpass filters are also used on the three images of the GOI to exclude light outside the range $350\text{-nm} \pm 5\text{-nm}$.

The higher sensitivity part of the forward scattered light instrument is an array of half-inch diameter mirror detectors. These detectors measure the low level of light scattered at large forward angles and are designed to have much higher sensitivity than the scatter plate. The detectors consist of concave mirrors placed at increasing angles from direct forward. Nine of the detectors are mounted to one extension arm and 5 additional detectors are mounted to a second arm at a

different azimuthal angle. Light incident on the detectors is reflected by the mirror surfaces and directed across the target chamber to a port on the opposite side. The light passes through focus partway across the chamber and emerges through a glass port as half-inch size spots. This light is then imaged with a focusing optic onto a Spectralon diffuser plate and the time-integrated signal is recorded with two CCD cameras. A bandpass filter limits the light detection to the spectral range of 350-nm \pm 5-nm for both cameras. Use of two cameras with a factor of 8 different intensity filtering increased the dynamic range of the data. Mirror detectors at the smallest angles were uncoated and mirrors at larger angles were aluminized in order to give comparable signal levels.

Azimuthal variation of the forward scattered light is not expected to be observable at small forward angles. However, polarization of the incident laser is expected to produce scattering which is stronger for forward angles out of the plane of incident laser polarization. The ratio between in-plane and out-of-plane scattering is estimated to be about 0.75 at a 30° forward scattering angle. The two sets of mirror detectors showed a signal ratio which, on average, was not less than the estimated 0.75 value.

In addition to the mirror detectors there are 6 fibers placed at a range of angles relative to the scatter plate. Two of the fibers are located behind the main scatter plate and 4 extend in angle out from it. The fibers carry light to the input of a 1-m spectrometer which disperses the light and images it onto the photocathode of a streak camera which records the time history of the spectrum. The output signal is spectrally resolved to about 0.7 Å and temporally resolved to about 30 ps.

4. 263-nm probe and forward scattered light measurements

Measurements of the forward scattered light from a 263-nm low intensity probe laser[28] are made with 400 μ m optical fibers positioned at six angles in the forward direction between 2° and 10°. The total incident energy of this beam is about 40 J in 1 ns. The resulting focused intensity is $\leq 1 \times 10^{14}$ W/cm² which is too low

to perturb the local plasma parameters. We cannot spectrally resolve the small frequency shifts in the forward scattering of this light so the light from the fibers is passed through a 263-nm narrow bandpass filter and then directly onto the active surface of a fast photodiode. The fibers have staggered lengths so that the signals can be multiplexed onto one scope channel. The fiber transmission from detector to output is calibrated in-situ with a narrow-band filtered Xe source lamp. The diode is absolutely calibrated with a separate 263-nm laser. The resulting signals show the brightness of the forward scattered light from the 263-nm laser.

B. Experimental results of intrinsic fluctuations

1. Forward scattered light amplitude

Figure 2 shows the time-integrated forward light signal for the 351-nm beam with KPP smoothing only and then for KPP with SSD and PS for two plasma densities. The error bars indicate the uncertainty in the half-inch mirror detector calibration. The time resolved signal from the fibers[24] shows that most of the scattering occurs while both the heater and probe beams are on (from 0.5 to 1 ns); the scattering amplitude decreases by about a factor of two to three after the heating pulse turns off. The ordinate in the plots is $J_{\text{scat}}/\text{sr}$ normalized to the incident beam energy. A laser shot through chamber center with no target present would result in all of the laser power propagating to the scatter plate where it would illuminate a region on the plate corresponding to the near-field size of the f/8.5 cone. The forward signal amplitude in this case is one over the number of steradians in the f/8.5 beam cone or about 90. The signal value is typically 30 or less with a target present; the reduction from 90 is primarily the result of inverse bremsstrahlung absorption. The data shows both small-angle and large-angle spreading. Small-angle spreading causes the incident f/8.5 beam to broaden by about a factor of 2 in angle (to 7°). The angular fall-off out to 7° is determined using the measured 2-D gated image of the scatter plate. The energy fraction outside of the 7° cone is

about 15 to 30% of the total transmitted light for KPP smoothing only. Addition of SSD and PS beam smoothing reduces the large-angle scattered light.

As a way of evaluating the significance of this beam spray for ignition hohlraums we conducted several simulations. For example, we used approximately twice the measured level of beam spray from the gasbag experiments and applied this to all 192 NIF laser beams in an ignition hohlraum simulation. We found that asymmetries in the x-ray illumination of the capsule resulted from the redistribution of laser light due to beam spray. If left uncorrected these asymmetries led to significantly lower fusion yield. However, further simulations showed that it was possible to adjust the relative power in the laser beams while keeping the total power into the hohlraum fixed so as to recover high yield from the target capsule. This shows that it is important to understand beam spray in hohlraum plasmas in order to be able to optimize NIF performance for ignition.

2. Forward scattering of the 263-nm probe

Experimental measurements indicate that the large angle spreading of the forward scattered light results from fluctuations induced by the high intensity probe beam. The small angle spreading, on the other hand, seems to result from a background fluctuation spectrum likely resulting from the heater beams. Separate measurements of the forward scattering with a low intensity 263-nm beam which passed only through the gasbag plasma heated by the heater beams confirmed this hypothesis. This beam does not generate its own density perturbations so the forward scatter can only result from background fluctuations. Figure 3 shows the angular fall-off in the transmitted 263-nm beam for two different plasma densities. We did not measure the angular dependence of the probe beam for $\theta < 2.4^\circ$ so we show a constant value in this region based on an estimate (error of $\pm 10\%$) of the probe transmission. We obtain this estimate by scaling the measured 351-nm transmission using the expression for inverse bremsstrahlung absorption. These measurements are interpreted in Section IV C.

3. Forward scattered light spectrum

The spectrum of the scattered 351-nm beam exhibits spectral broadening and has a red shift which increases with angle. The red shift at low intensity, shown in Fig. 4 (a) for f/4.3 and f/8.5 beams, increases with forward angle in a similar way as the classical SBFS[30-33] shift. This red-shift is given as $|\omega_0 - \omega_{sc}|/(k_0 C_s) = 2 \sin(\theta/2)$ where θ is the angle from the forward direction, ω_0 is the probe frequency, ω_{sc} is the scattered frequency, k_0 is the incident wavenumber, and C_s is the ion sound speed. The value of C_s is determined from the measured backscattered red shift ($\Delta\lambda/\lambda = 2.56 \times 10^{-3} = 2C_s/c$ where c is the speed of light). Figure 4 (a) also shows the red shift for a high intensity f/4.3 beam at $\langle I \rangle \sim 8 \times 10^{15} \text{ W/cm}^2$. Strongly driven SBFS is the most likely explanation for the increased red shift since simple considerations can rule out explanations involving probe-plasma heating and self-phase modulation. The intensity required to give the increased red shift from strongly driven SBFS is estimated from the dispersion relation[29, 30] to be $I \sim 1 \times 10^{16} \text{ W/cm}^2$ for scattering at 20° . The 351-nm beam has $\sim 70\%$ of its energy in speckles at or above $1 \times 10^{16} \text{ W/cm}^2$. In light of this we conclude that classical or strongly driven SBFS is the primary physics process which creates the majority of the 351-nm forward scattered light beyond 7° .

Figure 4 (b) shows that the plasma-induced spectral width depends on angle and intensity. The measured spectrum is fit with a Gaussian and the width is defined as the Gaussian full width at half maximum (FWHM). The measured instrument resolution of $\Delta\omega/k_0 C_s = 0.14$ (0.7\AA) has been deconvolved from the values plotted in Fig. 4 (b). Plasma-induced bandwidth can result from finite beam width, filamentation, multiple scattering from SBFS, scattering from background density fluctuations, and damping of SBFS. There is no reason to rule out any of these at the present time and we must wait for further measurements to determine the relative importance of each effect. In spite of our uncertainty as to the origin of the bandwidth, we conclude that the bandwidth of the laser increases by 1\AA after

traversing the plasma. This is enough to help reduce the growth of laser-plasma instabilities in the region beyond where the bandwidth develops[29].

II. Driven fluctuations

Driven fluctuations refer to the case when the target composition or laser intensity spatial variation are selected for the purpose of creating a particular scalesize fluctuation in the plasma. Scattering experiments with foam targets showed that the initial regular internal target structure caused density perturbations of similar scalesizes in the resulting plasma. We conducted exploding foil experiments which showed that a spatially periodic intensity variation produced density fluctuations with the same spatial periodicity.

A. Foam target experiments

The foam targets were composed of either glass (SiO_2) or plastic (CH). The glass foam, called aerogel, had an average cell size of $0.5\mu\text{m}$ (comparable to the $0.351\mu\text{m}$ laser wavelength) and the CH foam, called agar, had a much larger average cell size of about $5\mu\text{m}$. Both foams had an average mass density of 3 mg/cm^3 . Figure 5 shows electron micrographs of the two foams studied in the forward scattering experiment. When fully ionized the agar foam gave an electron density of 11% critical for 351-nm light and the aerogel foam was 9% critical electron density. The foam experimental setup is shown in Fig. 1 (b) and the forward scattered light signal was measured using the same detector as was used in the gasbag experiments.

The aerogel spacing is close to the $0.351\mu\text{m}$ laser light wavelength and is therefore expected to scatter the light by a larger angle than the agar. Only one Nova beam is used for the experiment so that the forward scattered light signal is weaker than in the gasbags due to substantial energy absorption during the initial heating process. The angular distribution of light scattered from the agar foam ($5\mu\text{m}$ cell size) falls off rapidly with increasing forward angle as shown in Fig. 6. On the other hand, the aerogel foam ($0.5\mu\text{m}$ cell size) shows a nearly constant level of angularly spread light as far out as the last detector at 35° .

The spectral data for the foams shows a broad essentially unshifted signal as opposed to a red or blue shifted signal. This spectral information indicates that the scattering is from the foam structure rather than being excited by forward scattering instabilities.

B. Trident exploding foil experiments

1. Trident laser

The exploding foil experiments were conducted using the Trident laser at the Los Alamos National Laboratory[34]. The Trident laser is a Nd:glass laser that operates at 1053-nm. The laser has two beams which can achieve about 250 J of 1053-nm energy in 1-ns and a third beam which is used for probing purposes. This beam is typically operated at energies up to 40 J. The experiments discussed here used the high energy beams at the second harmonic (527-nm) in a 2-nm square pulse shape with f/6 focusing optics. The low energy beam was operated in the 10 to 100 mJ range of third harmonic (351-nm) laser light in a 100 ps pulse and was configured as an f/100 beam.

2. Experimental setup and targets

Exploding foil targets composed of 1 to 2.5 μm of Mylar (CHO) were used to create the plasma. The experiments explored two heater beam configurations shown in Fig. 7 (a) and (b). In one case a wedge was placed in half of a single f/6 heater beam having 180 J in 2-ns of 527-nm light causing the beam to interfere with itself. Other techniques for creating an interference pattern at the target have been used before in separate exploding foil experiments[35,36]. The angle of interference between the two beam halves is the half-angle of an f/6 beam or 4.8° . The resulting intensity at the target for perfect beams is given as $4I_0 \sin^2[k_0 y \sin(4.8^\circ/2)]$ where I_0 is the average intensity of the non-interfering beams, y is the direction of the interference modulation (transverse to the beam propagation direction), and k_0 is the wavenumber of the laser. The target was illuminated with the resulting

500 μm by 250 μm focal spot having a 6.3 μm intensity modulation. This beam burned through the foil and heated the resulting plasma to about 700 eV. At 1-ns a low energy (10-100 mJ) f/100 probe beam at 351-nm and a 100-ps wide Gaussian pulse was directed across the original surface of the foil at a height of 200 μm in a transverse direction to the heater beam. The second heater beam configuration [Fig. 7 (b)] consisted of creating a higher spatial frequency modulation (1.3 μm) in the intensity by interfering 2 separate heater beams, 23° apart, at the target surface. The energy in each heater beam in this case was about 80 J. The main diagnostic for this experiment consisted of an f/1 mirror placed about 6 inches from the target and oriented normally to the 351-nm probe beam in the forward direction. Additional optics imaged the surface of this mirror onto a CCD camera which recorded the forward scattered 351-nm light signal. Thomson scattering measurements diagnosed the temperature of this plasma.

3. Laser-driven fluctuation experimental results

We verified the resulting interference pattern created by the wedge in the first heater beam configuration using an alignment beam. The 0.351 μm probe beam, which propagates transversely to the heater beam, is expected to be deflected in two opposing directions by 3.1° based on k -matching the probe and the expected imposed density fluctuation. Figure 8 shows the forward scattered light from the probe beam when the foil is illuminated with a self-interfering heater beam (a) and when the wedge is removed giving no interference pattern (b). The images are time integrated and show the spatial distribution of forward scattered light from the probe beam at the location of the collection mirror. The view in the figures is directed at the collection mirror. An oversized sketch of the foil target shows its original location. An opaque strip was placed on the surface of the collection mirror to block the bright straight-through probe light. The location of this strip is indicated in the images with two horizontal dotted lines. Moving away from the target in the images corresponds to increasing forward scattering angle. Figure

8 (a) shows two dim signals, one above and the other below the target sketch at equal angles corresponding to scattering at 3.1° . In addition to these dim signals is a brighter signal showing light emerging from the obscuration due to refraction by the exploding foil plasma. This cannot be filamentation-induced beam bending because the beam intensity is too low to filament and/or backscatter ($I \leq 1 \times 10^{13} \text{ W/cm}^2$). The energy of light scattered into the dim spots at $\pm 3.1^\circ$ is estimated to be 1.2×10^{-4} of the main incident energy. Removing the wedge changes the self-interference pattern to a circular spot on the target measuring $500 \mu\text{m}$ in diameter. To keep the average intensity of the circular spot (no wedge) similar to the spot with the wedge, the beam focus was adjusted to decrease the circular focal spot to a $350 \mu\text{m}$ diameter. The scattered light signal without the wedge is shown in Fig. 8 (b). It does not show the two dim signals seen in Fig. 8 (a) but still shows the refracted light. The filtering for the camera and the incident energy of the probe are the same for both images. The refracted signal varied somewhat on a shot-to-shot basis. Installing and removing the wedge was repeated several times and each time we found that the two dim spots at $\pm 3.1^\circ$ were present with the wedge but were not observable without the wedge.

The second heater beam configuration did not show evidence of probe laser scattering; the scattering angle in this case is 15.3° . This configuration should produce an interference pattern on the target with a separation of $1.3 \mu\text{m}$ between intensity maxima. We were not able to verify the interference pattern at the target but verified that the beams overlapped, that they arrived at the target simultaneously, that they were temporally coherent at the target, and that their polarizations were aligned. We did not observe any scattered light fraction above 10^{-5} of the incident light. Measurements of the heater beam uniformity at 2 to 3 mm from best focus show 20 to 30% intensity variations over a distance of about $100 \mu\text{m}$ and phase variations of about π over similar distances. We did not observe any fine scale speckle structure in the heater beams at these large defocus distances. It is possible that the low density plasma which the heaters must pass through before

reaching the location of the probe beam may create fine scale speckle structure in the beam due to laser-plasma interactions. Ability to gradually increase the heater beam interference angle from 4.8° to 15.3° could help identify the reason no large angle scattered light was observed in this second heater beam configuration.

IV. Modeling

The goal in modeling these experiments is to infer from the forward scattered light a plasma density fluctuation (PDF) spectrum which, when used in our scattering model, gives a calculated forward scattered light signal which matches the measured forward scattered light signal. We do not attempt to describe from first principles the detailed process whereby filamentation/SBFS or other low frequency processes lead to this fluctuation spectrum.

A. Wave kinetic equation

The fluctuations causing the observed forward scattering are low-frequency [$|\omega - \omega_0|/\omega_0 < 9 \times 10^{-4}$ from Fig. 4 (a)] so they can be considered stationary for the purpose of calculating the angular scattering. The method for inferring the fluctuation spectrum is to first prescribe the shape and amplitude of a stationary PDF spectrum $S(k)$. The spectral amplitude is normalized to a mean-square fluctuation level, defined as $\langle |\delta n/n|^2 \rangle \equiv \int S(k) d^3k$, where the plasma density is written as $n_e = n + \delta n$ and n is the average electron density. Next, we compute the scattered light distribution resulting from this PDF spectrum using a wave kinetic equation. The calculated scattered light is compared to the measured light and the spectrum is adjusted to bring the calculation into agreement with the measurement. This technique provides a way to determine the general characteristics of the fluctuation spectrum.

The first step in obtaining the wave kinetic equation is to consider an electromagnetic wave propagating through a varying density plasma. The electric field part of the electromagnetic wave evolves according to the wave equation

$$\nabla^2 E - \frac{1}{c^2} \frac{\partial^2 E}{\partial t^2} = \frac{\omega_{p0}^2}{c^2} (1 + \delta n/n_0) E \quad (1)$$

where E is the electric field, c is the speed of light, and the nonuniform density, δn , only varies in space and not in time. The only time dependence enters through the frequency of the electric field which is written as $E(r, t) = E(r) \exp[-i\omega_0 t]$ where ω_0 is the oscillation frequency of the field. We assume that the scattering is weak so that power is scattered out of the main beam slowly compared to the rapid variation in the phase of the electric field along the direction of propagation which we take to be z . This allows us to make the envelope approximation and write the electric field as $E(r) = E(x, y, z) \exp[ik_0 z]$. Making the paraxial approximation and assuming that diffraction can be neglected gives the first order equation for the envelope, E , which is written as

$$\frac{\partial E}{\partial z} = \frac{-i}{2k_0} \frac{\omega_p^2}{c^2} \frac{\delta n}{n_0} E. \quad (2)$$

This equation has the solution

$$E(z) = E_0 \exp \left[\frac{-i}{2k_0} \frac{\omega_p^2}{c^2} \int_0^z dz' \frac{\delta n}{n_0} \right]. \quad (3)$$

This solution for the electric field shows that density inhomogeneities in the plasma create perturbations to the electric field phase. This process is shown schematically in Fig. 9.

Equation (3) is an intermediate step in obtaining the wave kinetic equation which describes the angular distribution of power or energy. The speckle structure of the beam creates many locations in the plasma, each statistically independent from the others, which produce forward scattered light. The total scattered light is therefore equal to an ensemble sum of random phased scatterers each obeying Eq. (3). Following a similar procedure as outlined in Refs. [37-39] we use Eq. (3) to derive an expression for the transverse spectrum of the ensemble-summed power as a function of propagation distance through the plasma; this is the wave kinetic equation. We start with the power defined in terms of the electric field as

$$P_{ij}(z) = \frac{c}{8\pi} |E_{ij}(z)|^2 \quad (4)$$

where

$$E_{mn}(z) = \frac{1}{L_x} \frac{1}{L_y} \int dx \int dy E(x, y, z) \exp(-ik_{xm}x - ik_{yn}y), \quad (5)$$

$k_{xm} = 2\pi m/L_x$, $k_{yn} = 2\pi n/L_y$, and m and n are integers. Writing $E_{ij}(z)$ in Eq. (4) as an ensemble sum of fields and then using Eqs. (3) and (5) leads to the wave kinetic equation for $P_{ij}(z)$ which is written as

$$\frac{dP_{ij}}{dz} = \left(\frac{1}{2k_0} \frac{\omega_p^2}{c^2} \right)^2 \left[\sum_{lm} P_{i-l, j-m} S_{lm} - \sum_{uv} P_{ij} S_{u-i, v-j} \right]. \quad (6)$$

Here S_{ij} is the 2-D surface within the spectral energy density of the fluctuations which satisfies $|k_0 + \Delta k_{ij}| = |k_0|$. This condition preserves the magnitude of the electromagnetic wavenumber in a scattering event. If the laser $|k_0|$ is large compared to the Δk_{ij} -values for which $S(\Delta k_{ij})$ is significant then this surface is essentially a plane defined by $k_0 \bullet k_{ij} = 0$. The density fluctuation amplitude is related to S_{ijl} as

$$\langle |\delta n/n|^2 \rangle = \sum_{ijl} S_{ijl} \quad (7)$$

B. Methods for solving the wave kinetic equation

The first term in Eq. (6) for dP_{ij}/dz represents the rate at which power is scattered into P_{ij} and the second term describes the rate at which power is scattered out of P_{ij} . The distance, Δz , required to scatter all of the initial power out of P_{ij} into other components is estimated from Eq. 6 to be

$$(\Delta z)^{-1} = \left(\frac{1}{2k_0} \frac{\omega_p^2}{c^2} \right)^2 \sum_{uv} S_{u,v}. \quad (8)$$

This distance is about 8 to 15 mm for scattering from probe-driven fluctuations (2 to 4 μm scalesize). Background fluctuations ($> 40 \mu\text{m}$ scalesize) reduce this scattering distance by about a factor of 10. This means that in a gasbag plasma measuring 2.5 mm across that about 15 to 30% of the light experiences one scattering event from fluctuations associated with the probe beam and about 95% of the light scatters from

the background fluctuations. Multiple scattering events therefore have a significant probability and cannot be ignored.

Equation 6 is easily adapted to a Monte Carlo ray tracing solution technique. The technique consists of launching a large collection of rays corresponding to the incident laser k -spectrum. The second term in Eq. (6) gives the rate and direction that rays are scattered as they propagate through the fluctuating plasma. These rays are advanced in the direction of their instantaneous k by a stepsize chosen so that the scattering probability in this step is small and is given by

$$P_{scat} = (\Delta z)_{step} \left(\frac{1}{2k_0} \frac{\omega_p^2}{c^2} \right)^2 \sum_{uv} S_{u,v}. \quad (9)$$

A random number, R , ranging between 0 and 1 is generated for each ray. The ray is advanced another step in the same direction unless the random number is less than P_{scat} . In this case the ray is scattered. A scattering event changes the direction of the ray's k -vector (so that $k_{scat} = k + \Delta k$) and then the ray is advanced again. The size and orientation of Δk is chosen randomly but has a probability distribution with the same shape as S_{ij} . One disadvantage of the Monte Carlo technique is that it requires many rays to achieve good statistics at scattering angles where the scattered light fraction is very low. We have also solved Eq. 6 analytically and show the result in Appendix I. The analytical solution is useful as a check on the Monte Carlo calculation and provides more accurate scattered light calculations in the regions where the scattering amplitude is small.

C. Intrinsic fluctuation modeling

The gasbag results show evidence of both small and large-angle scattering. As was discussed earlier, this observation suggests a two component fluctuation spectrum. The small-angle scattered light can be produced with a small- k fluctuation and the light at larger angles requires a larger- k fluctuation. We constructed a spectrum having these two components and then varied the parameters describing the spectrum in order to match the data. The spectrum we chose has a constant

value for $0 \leq k \leq k_s$ (small- k part) then changes to a different constant value for $k_s \leq k \leq k_l$ (large- k part). This spectrum is defined analytically using 4 parameters: 1) the magnitude of $\langle |\delta n/n| \rangle$, 2) the extent of the small- k part of the spectrum (k_s), 3) the extent of the large- k part of the spectrum (k_l) and 4) the ratio of the large- k and small- k part. A parameter scan of these quantities led to the spectrum shown in Fig. 10 (a) which matches the scattered light data at low density [Fig. 2 (a)]. The total fluctuation amplitude is $\langle |\delta n/n| \rangle = 0.08$. Adding SSD and PS reduces the large- k part of the spectrum a factor of 10 reducing the total fluctuation amplitude to $\langle |\delta n/n| \rangle = 0.06$. The small-angle beam spreading is not significantly affected by addition of beam smoothing.

It is difficult to fit the high density data with a similar two-part constant spectrum. However, we found that we could match the data if we used a decreasing exponential rather than a constant value for the large- k part. The actual spectra used to fit the high density data is shown in Fig. 10 (b). The KPP-only spectrum consists of a flat small- k region extending to $k/k_0 = 0.03$ (slightly more than in the low density case) and a decaying exponential with the analytical form $7 \times 10^{-4} \exp(-10k/k_0)$. Applying beam smoothing decreases the exponential part by 3.5 times. The total fluctuation amplitude is $\langle |\delta n/n| \rangle = 0.07$ with no smoothing and decreases to $\langle |\delta n/n| \rangle = 0.05$ with the addition of SSD and PS.

It is possible to fit the data at low density with a decreasing exponential rather than a two-part flat spectrum. Comparing the flat and decreasing exponential spectra that correctly fit the low density data we see that both spectra exhibit the common features of a small- k part and a large- k part. The main distinction is the transition between the two spectral regions. Since we infer the spectra from the data the spectral details are not determined uniquely. There may still be other spectra which also fit the data.

The modeling does not uniquely determine the longitudinal character of the fluctuation spectrum. Nevertheless, we have taken the spectrum in the calculation to be isotropic. This results in an upper bound to the fluctuation level. There are

several reasons for making the isotropic assumption. First, the background spectrum appears to come from the heater beams; since these beams are approximately isotropic we expect the density perturbations created by them to also be isotropic. Second, the probe-induced density perturbations seem to arise mainly from SBFS. This instability grows exponentially in space so that the largest amplitude correlated density perturbation due to the ion wave is largest in the last e-fold of growth. This is a localized region which we've taken to be on the order of an f/8 speckle width (about 4 μm). There is no data available to indicate the true longitudinal correlation length of the fluctuations. If the correlation length is longer than an f/8 speckle width then the calculated density fluctuation amplitude will be reduced. For a fixed scattered power the fluctuation amplitude scales as $1/\sqrt{l_c}$ where l_c is the longitudinal correlation length.

The same wave-kinetic equation used to predict the angular spreading for the 351-nm beam is used to calculate the spreading of the 263-nm beam. We find that using only the small- k part of the spectrum found in the low density 351-nm case can explain the measured angular fall-off of the 263-nm light. The amplitude of $\langle |\delta n/n| \rangle$ for both low and high density plasmas is 0.05. Comparison of the calculated scattered light and the measured light shows good agreement at both low and high electron density as seen in Fig. 3.

D. Driven fluctuation modeling

1. Foam modeling

Applying the same wave kinetic model to the foam measurements leads to the two spectra shown in Fig. 11 Both foams show spectra that roughly match the scalesize of the initial density perturbations given by the foam cell size. The calculated fluctuation amplitude in the agar is $\langle |\delta n/n| \rangle = 0.08$ but in the aerogel it is $\langle |\delta n/n| \rangle = 0.2$.

The duration of the aerogel signal is about 600 ps and about 300 ps for the agar foam for a 1 ns laser pulse. We speculate on the reason for the shortened

signal duration as follows. The large density structures in the foams only produce scattering for several ion acoustic damping times (while the fluctuations are large). The damping time is determined by the foam composition and the cell size and is 33 ps for both foams. The density perturbations at one location actively scatter for perhaps three e-folds (~ 100 ps) before the scattered light level at this location becomes insignificant. The interaction beam takes 200 to 400 ps to burn through the 1 to 1.5 mm thick foam. Thus, significant forward scattered light signal is expected to last for 300 to 500 ps which is close to what is observed in the experiment.

2. Exploding foil modeling

The first heater beam configuration used the wedge to construct an interference pattern at the target of $6.3\mu\text{m}$. Measurements, as described before, indicate a transverse correlation length at the target of about $100\mu\text{m}$. The expected scattering angle obtained by k -matching the $0.351\mu\text{m}$ probe with the interference pattern is 3.1° . Figure 8 (a) shows a forward scattered light signal at both $+3.1^\circ$ and -3.1° with the wedge installed. Removing the wedge causes the scattered light at the $\pm 3.1^\circ$ to vanish as seen in Fig. 8 (b). The measured angle agrees with the expected scattering angle within the measurement error. This result gives evidence that the intensity modulation pattern due to the wedge is impressed on the plasma.

Figure 8 (a) also shows that the scattered light amplitude (estimated from the measured signal and a calibration signal) normalized to the incident energy is 1.2×10^{-4} . This level of light can be used in the scattering model to make an estimate of the amplitude of $\langle |\delta n/n| \rangle$. The plasma density is 5% of critical for 527-nm light (2.2% critical for 351-nm). The heater beam is assumed to remain correlated over $75\mu\text{m}$ in the transverse and longitudinal directions (reduced from the measured $100\mu\text{m}$ in anticipation of some plasma-induced decorrelation). Figure 12 (a) shows the calculated scattered light for $\langle |\delta n/n| \rangle = 0.002$; the signal amplitude at $\pm 3.1^\circ$ is the same amplitude as measured in the experiment. If the scattered light fraction is small compared to unity then it is proportional to the

product $(k_0 L_z)(k_0 l_c)(n/n_c)^2 < |\delta n/n|^2 >$ where L_z is the length of the overall region where scattering occurs and l_c is the longitudinal correlation length of the density perturbation. This expression can be used to scale the calculated density perturbation for different values of l_c or L_z . Figure 12 (b) is a sketch of the density fluctuation power spectrum used in the calculation of the scattered light in Fig. 12 (a). The spectrum consists of two small scattering centers at $\pm 0.054k_0$ with size determined by the transverse and longitudinal correlation lengths of the fluctuations.

The density perturbation estimated by balancing the ponderomotive pressure from the imposed intensity pattern with the plasma thermal pressure is given as $0.25v_{os}^2/v_{th}^2$ where v_{os} is the quiver velocity of the electrons and v_{th} is the electron thermal velocity. This can be written as $\delta n/n \sim 9 \times 10^{-3}[I\lambda^2/T_e]$ where the laser intensity, I , is divided by $1 \times 10^{14} \text{ W/cm}^2$, the laser wavelength, λ , is in microns, and the electron temperature, T_e , is in keV. The intensity at the peaks in the interference pattern is approximately $1 \times 10^{14} \text{ W/cm}^2$. Using $0.527 \mu\text{m}$ for the wavelength and 0.7 keV for the electron temperature (estimated from Thomson scattering) gives $\delta n/n = 4 \times 10^{-3}$ which is within a factor of two of the estimate using the scattering model. This indicates that our estimates for the correlation lengths are reasonable; a factor of two error in the density fluctuation amplitude corresponds to a factor of 1.4 in one of the correlation lengths or the propagation distance.

The second heater beam configuration did not produce measurable scattered light at the expected angle of 15.3° . This configuration used two f/6 heater beams at 23° center-to-center to form an interference pattern with a $1.3 \mu\text{m}$ peak-to-peak spacing. During the experiment we confirmed that the beam timing and polarization between the two heater beams were correct for creating an interference pattern. We varied the intensity of the heater spot by varying the energy in the beams and by changing the spot size. None of these changes led to a clear scattered light signal at 15.3° .

There are several reasons which may account for this result. Phase perturbations introduced by the plasma may cause the expected interference pattern to form without sufficient spatial coherence to scatter a detectable amount of light. Another possibility is that at the larger scattering angle k -matching may not be sufficiently satisfied in the experimental geometry resulting in a reduced scattering efficiency. The density perturbation k -vector is oriented 90° relative to the probe beam k -vector. Exact k matching requires an angle between the probe beam and the density perturbation k -vectors of 97.7° or 82.3° . Resolution of this result awaits further experimental investigation.

V. Summary

We have described experiments investigating intrinsic and controlled fluctuations in different types of laser-produced plasmas. The aim of the gasbag experiments was to study the fluctuation spectrum and forward scatter which results from 9 heater beams and one higher intensity probe beam illuminating a plasma having similar density and scalelength as the central region of a NIF hohlraum. The results show small angle and large angle beam spread in the forward direction. This can only be explained with a density fluctuation spectrum having both small and large- k components. Frequency measurements indicate that the forward scattering arises from stimulated Brillouin forward scattering (SBFS) and filamentation. A model which calculates the scattering from a given fluctuation spectrum shows agreement with the measurements for a fluctuation amplitude of $\langle |\delta n/n| \rangle = 0.08$ and a spectral shape having a large- k and small- k part. Adding SSD and polarization smoothing leads to a reduction in the large angle scattering giving $\langle |\delta n/n| \rangle = 0.06$. This almost recovers the background level which is separately determined to be $\langle |\delta n/n| \rangle = 0.05$ using the forward scatter from a 263-nm low intensity probe beam.

Experiments using foam targets with two different cell sizes show evidence of initial target structure in the resulting plasma which is observable with forward

scattered light. Time-dependent measurements of forward scattered light indicate the rate at which the initial density perturbations smooth out in a foam target. Analysis of the data with the scattering model shows that the scattered light can be explained using fluctuation spectra with scalelengths similar to the initial cell size of the foams.

Exploding foil experiments using the Trident laser show that an intensity pattern creates a correlated density perturbation with an estimated amplitude that agrees with simple ponderomotive force estimates. This result confirms our understanding of how a moderate intensity laser creates a density perturbation. This result can be useful for developing more sophisticated models of laser propagation through a plasma.

The author gratefully acknowledges useful discussions with P. E. Young, B. B. Afeyan, S. N. Dixit, S. M. Pollaine, A. M. Rubenchik and the help of R. Griffith with the streak camera instrument. This work is performed under the auspices of the U. S. Department of Energy by the Lawrence Livermore National Laboratory under Contract No. W-7405-ENG-48.

Appendix 1.

The wave kinetic equation for $P_{ij}(z)$ is written as

$$\frac{dP_{ij}}{dz} = \left(\frac{1}{2k_0} \frac{\omega_p^2}{c^2} \right)^2 \left[\sum_{lm} P_{i-l,j-m} S_{lm} - \sum_{uv} P_{ij} S_{u-i,v-j} \right] \quad (10)$$

where S_{ij} is the 2-D surface within the spectral energy density of the fluctuations which satisfies $|k_0 + k_{ij}| = |k_0|$. It is possible to solve this kinetic equation in closed form. The solution is readily obtained by first transforming it to spatial coordinates in the transverse direction. This gives

$$\frac{dP}{dz} = \left(\frac{1}{2k_0} \frac{\omega_p^2}{c^2} \right)^2 P \left[\bar{S} - S_0 \right] \quad (11)$$

where

$$\bar{S}(x, y) = \sum_{pq} S_{pq} \exp(-ik_{xp}x - ik_{yq}y), \quad (12)$$

and $S_0 = \bar{S}(x = 0, y = 0)$. This ordinary differential equation for P has the solution

$$P(x, y, z) = P_0(x, y) \exp \left[z \frac{k_0^2}{4} \left(\frac{n}{n_c} \right)^2 \left(\bar{S}(x, y) - S_0 \right) \right] \quad (13)$$

where $P_0(x, y)$ is the incident power function, z is the propagation distance, and ω_p^2/c^2 has been rewritten as $(n/n_c)k_0$. Transforming (x, y) back to wavenumbers (i, j) gives the solution for $P_{ij}(z)$ which is written as

$$P_{ij}(z) = \sum_{lm} P_{0i-l, j-m} \frac{1}{L_x L_y} \int dx dy \exp(-ik_{xl}x - ik_{ym}y) \exp \left[z \frac{k_0^2}{4} \left(\frac{n}{n_c} \right)^2 \left(\bar{S}(x, y) - S_0 \right) \right]. \quad (14)$$

REFERENCES

1. A. V. Maximov, W. Rozmus, V. T. Tikhonchuk, D. F. DuBois, H. A. Rose, and A. M. Rubenchik, *Phys. Plasmas* **3**, 1689 (1996).
2. B. B. Afeyan, A. E. Chou, J. P. Matte, R. P. J. Town, and W. J. Kruer, *Phys. Rev. Lett.* **80**, 2322 (1998).
3. D. S. Montgomery, B. B. Afeyan, J. A. Cobble, J. C. Fernandez, M. D. Wilke, S. H. Glenzer, R. K. Kirkwood, B. J. MacGowan, J. D. Moody, E. L. Lindman, D. H. Munro, B. H. Wilde, H. A. Rose, D. F. Dubois, B. Bezzerides, H. X. Vu, *Phys. Plasmas* **5**, 1973 (1998).
4. J. D. Moody, B. J. MacGowan, S. H. Glenzer, R. K. Kirkwood, W. L. Kruer, A. J. Schmitt, E. A. Williams, and G. F. Stone, *Phys. Rev. Lett.* **83**, 1783 (1999).
5. J. D. Lindl, *Phys. Plasmas* **2**, 3933 (1995).
6. S. W. Haan, S. M. Pollaine, J. D. Lindl, L. J. Suter, R. L. Berger, L. V. Powers, W. E. Alley, P. A. Amendt, J. A. Futterman, W. K. Levedahl, M. D. Rosen, D. P. Rowley, R. A. Sacks, A. I. Shestakov, G. L. Strobel, M. Tabak, S. V. Weber, G. B. Zimmerman, W. J. Krauser, D. C. Wilson, S. V. Coggeshall, D. B. Harris, N. M. Hoffman, and B. H. Wilde, *Phys. Plasmas* **2**, 2480 (1995).
7. S. H. Batha, H. A. Baldis, K. S. Bradley, R. P. Drake, K. Estabrook, T. W. Johnston, D. S. Montgomery, and R. J. Procassini, *Phys. Fluids B* **1**, 2596 (1993).
8. R. P. Drake, K. Estabrook, and R. G. Watt, *Phys. Plasmas* **4**, 1825 (1997).
9. R. L. Kauffman, L. J. Suter, C. B. Darrow, J. D. Kilkenney, H. N. Kornblum, D. S. Montgomery, D. W. Phillion, M. D. Rosen, A. R. Theissen, R. J. Wallace, and F. Ze, *Phys. Rev. Lett.* **73**, 2320 (1994).
10. B. J. MacGowan, B. B. Afeyan, C. A. Back, R. L. Berger, G. Bonnaud, M. Casanova, B. I. Cohen, D. E. Desenne, D. F. DuBois, A. G. Dulieu, K. G. Estabrook, J. C. Fernandez, S. H. Glenzer, D. E. Hinkel, T. B. Kaiser, D. H. Kanantar, R. L. Kaufman, R. K. Kirkwood, W. L. Kruer, A. B. Langdon, B. F. Lasinski, D. S. Montgomery, J. D. Moody, D. H. Munro, L. V. Powers, H. A. Rose, C. Rousseaux, R. E. Turner, B. H. Wilde, S. C. Wilks, and E. A. Williams, *Phys. Plasmas* **3**, 2029 (1996).
11. D. H. Kalantar, D. E. Klem, B. J. MacGowan, J. D. Moody, D. S. Montgomery, D. H. Munro, T. D. Shepard, and G. F. Stone, *Phys. Plasmas* **2**, 3161 (1995).

12. J. J. Denavit and D. W. Phillion, *Phys. Plasmas* **1**, 1971 (1994).
13. L. V. Powers, R. L. Berger, R. L. Kauffman, B. J. MacGowan, P. A. Amendt, C. A. Back, T. P. Bernat, S. N. Dixit, D. I. Eimerl, K. G. Estabrook, J. A. Harte, D. H. Kalantar, D. E. Klem, B. F. Lasinski, D. S. Montgomery, J. D. Moody, D. H. Munro, T. D. Shepard, L. J. Suter, R. E. Turner, and E. A. Williams, *Phys. Plasmas* **2**, 2473 (1995).
14. S. H. Glenzer, C. A. Back, K. G. Estabrook, B. J. MacGowan, D. S. Montgomery, R. K. Kirkwood, J. D. Moody, D. H. Munro, and G. G. Stone, *Phys. Rev. E* **55**, 927 (1997).
15. J. D. Moody, B. J. MacGowan, R. L. Berger, K. G. Estabrook, S. H. Glenzer, R. K. Kirkwood, W. L. Kruer, D. S. Montgomery, and G. F. Stone, Submitted to *Physics of Plasmas* September 1999.
16. S. N. Dixit, J. K. Lawson, K. R. Manes, H. T. Powell, and K. A. Nugent, *Optics Letters* **19**, 417 (1993); S. N. Dixit, M. D. Feit, M. D. Perry, and H. T. Powell, *Optics Letters* **21**, 1715 (1996).
17. S. N. Dixit, I. M. Thomas, B. W. Woods, A. J. Morgan, M. A. Henesian, P. J. Wegner, and H. T. Powell, *Appl. Opt.* **32**, 2543 (1993); J. W. Goodman, *Statistical Optics* (Wiley, New York, 1985).
18. S. Skupsky, R. W. Short, T. Kessler, R. S. Craxton, S. Letzring, and J. M. Soures, *J. Appl. Phys.* **66**, 3456 (1989).
19. "Phase Conversion Using Distributed Polarization Rotation," LLE Review **45**, 1-12 (1990).
20. K. Tsubakimoto, M. Nakatsuka, H. Nakano, T. Kanabe, T. Jitsuno, and S. Nakai, *Opt. Commun.* **91**, 9-12 (1992); K. Tsubakimoto, T. Jitsuno, N. Miyanaga, M. Nakatsuka, T. Kanabe, and S. Nakai, *Opt. Commun.* **103**, 185-188 (1993).
21. S. Pau, S. N. Dixit, and D. Eimerl, *J. Opt. Soc. Am. B* **11**, 1498 (1994).
22. E. Lefebvre, R. L. Berger, A. B. Langdon, B. J. MacGowan, J. E. Rothenberg, and E. A. Williams, *Phys. Plasmas* **5**, 2701 (1998).
23. J. D. Moody, B. J. MacGowan, B. B. Afeyan, S. H. Glenzer, R. K. Kirkwood, W. L. Kruer, S. M. Pollaine, A. J. Schmitt, E. A. Williams, and G. F. Stone, *Rev. Sci. Inst.* **68**, 1725 (1997).
24. J. D. Moody, B. J. MacGowan, B. B. Afeyan, S. H. Glenzer, R. K. Kirkwood, W. L. Kruer, S. M. Pollaine, A. J. Schmitt, E. A. Williams, and G. F. Stone, *Rev. Sci. Inst.* **70**, 677 (1999).

25. S. C. Wilks, P. E. Young, J. Hammer, M. Tabak, and W. L. Kruer, *Phys. Rev. Lett.* **73**, 2994 (1994).
26. P. E. Young, J. H. Hammer, S. C. Wilks, and W. L. Kruer, *Phys. Plasmas* **2**, 2825 (1995).
27. P. E. Young, *Phys. Plasmas* **2**, 2815 (1995).
28. S. H. Glenzer, T. Weiland, and J. Bowers, *Rev. Sci. Inst.* **70**, 1089 (1999).
29. A. J. Schmitt and B. B. Afeyan, *Phys. Plasmas* **5**, 503 (1998).
30. J. F. Drake, P. K. Kaw, *et al.*, *Phys. Fluids* **17**, 778 (1974).
31. C. J. McKinstrie, J. S. Li, and A. V. Kanaev, *Phys. Plasmas* **4**, 4227 (1997); Lal, *et al.*, *Phys. Rev. Lett* **78**, 670 (1997).
32. V. V. Eliseev, *et al.*, *Phys. Plasmas* **4**, 4333 (1997).
33. C. Labaune, H. A. Baldis, B. Cohen, W. Rozmus, S. Depierreux, E. Schifano, B. S. Bauer, and A. Michard, *Phys. Plasmas* **6**, 2048 (1999).
34. N. K. Moncur, R. P. Johnson, R. G. Watt, and R. B. Gibson, *Appl. Opt.* **34**, 4274 (1995).
35. P. E. Young, H. A. Baldis, R. P. Drake, E. M. Campbell, K. G. Estabrook, *Phys. Rev. Lett.* **61**, 2336 (1988).
36. P. E. Young, *Phys. Plasmas* **2**, 2815 (1995).
37. E. Ott, *Phys. Fluids* **22**, 1732 (1979).
38. E. Ott, B. Hui, and K. R. Chu, *Phys. Fluids* **23**, 1031 (1980).
39. P. T. Bonoli and E. Ott, *Phys. Fluids* **25**, 359 (1982).

FIGURE CAPTIONS

FIG. 1 (a) Schematic of the detection system for measuring the amplitude and spectra of the near forward scattered light. The $f/8.5$ beam is converted to an $f/4.3$ beam in some cases. (b) The foam experiments are conducted using one Nova beam and the same forward light detection system shown in (a).

FIG. 2 Measurement of the forward scattered light amplitude vs angle for (a) 7.5% critical plasma and (b) a 14% critical plasma. Symbols show data points and lines show the calculated scattering using the wave kinetic equation using the fluctuation power spectra in Fig. 10. Application of SSD and polarization beam smoothing reduces the large-angle scattered light component but does not significantly affect the small angle scattering.

FIG. 3 Angular fall-off of the forward scattered light from the 263-nm low-intensity probe beam (symbols) shown with the calculated fall-off for $< |\delta n/n| >= 0.05$ (dotted lines).

FIG. 4 (a) Red shift of the forward scattered light shows evidence for classical and strongly driven forward SBS. (b) Spectral width of the forward light shows that the plasma-induced bandwidth increases for a higher intensity probe. The plasma density is 7% critical.

FIG. 5 Electron micrographs of (a) agar foam and (b) aerogel foam. The cell size is approximately $5\ \mu\text{m}$ for agar and about $0.5\ \mu\text{m}$ for aerogel.

FIG. 6 The measured angular fall-off of scattered light from the two different cell size foams (symbols) shows rapid fall-off for the agar but almost constant scattering for the aerogel. The dotted lines show the wave kinetic calculation for scattered light using the spectra shown in Fig. 11.

FIG. 7 Experimental setup for the exploding foil experiments using the Trident laser facility for (a) a small interference angle between the beams (4.8°) and (b) a larger angle (23°) between the beams. Probe light is collected by a spherical concave mirror and directed to a CCD camera detector.

FIG. 8 The images show the spatial distribution of scattered light at the surface of the spherical collection mirror for the Trident experiment using the small-angle interference configuration [Fig. 7 (a)]. (a) Installing the wedge leads to two scattered light spots at 3.1° . (b) Removing the wedge causes the spots to vanish.

FIG. 9 Schematic showing that density perturbations in the plasma alter cause phase perturbations in the laser as it propagates through the inhomogeneous plasma density. These phase perturbations lead to angular scattered light at the location of the detectors.

FIG. 10 Spectra used in the wave kinetic equation to give a calculated scattered light signal which matches the measured forward scattered light for (a) a 7.5% critical density gasbag plasma and (b) a 15% critical plasma. The shaded triangle shows the approximate power spectrum of the incident f/8.5 laser beam.

FIG. 11 Spectra used in the wave kinetic equation to match the forward scattered light data for (a) the agar foam and (b) the aerogel foam. Both spectra have a small- k background with an exponentially decaying part having a width corresponding to the cell size of the different foams. The shaded triangle shows the approximate power spectrum of the incident f/4.3 laser.

FIG. 12 (a) Plot showing the calculated forward scattered light using the fluctuation power spectrum shown in (b) with an amplitude of $\langle |\delta n/n| \rangle = 0.002$. The fluctuations produce two scattered light components at $+3.1^\circ$ and -3.1° . The shape of the fluctuation power spectrum is shown in k -space in (b). The spectrum is nonzero in a localized region around $\pm 0.054k_0\hat{z}$; the extent of this region corresponds to the correlation length of the interference pattern producing the fluctuations.

Figure 1 (a)

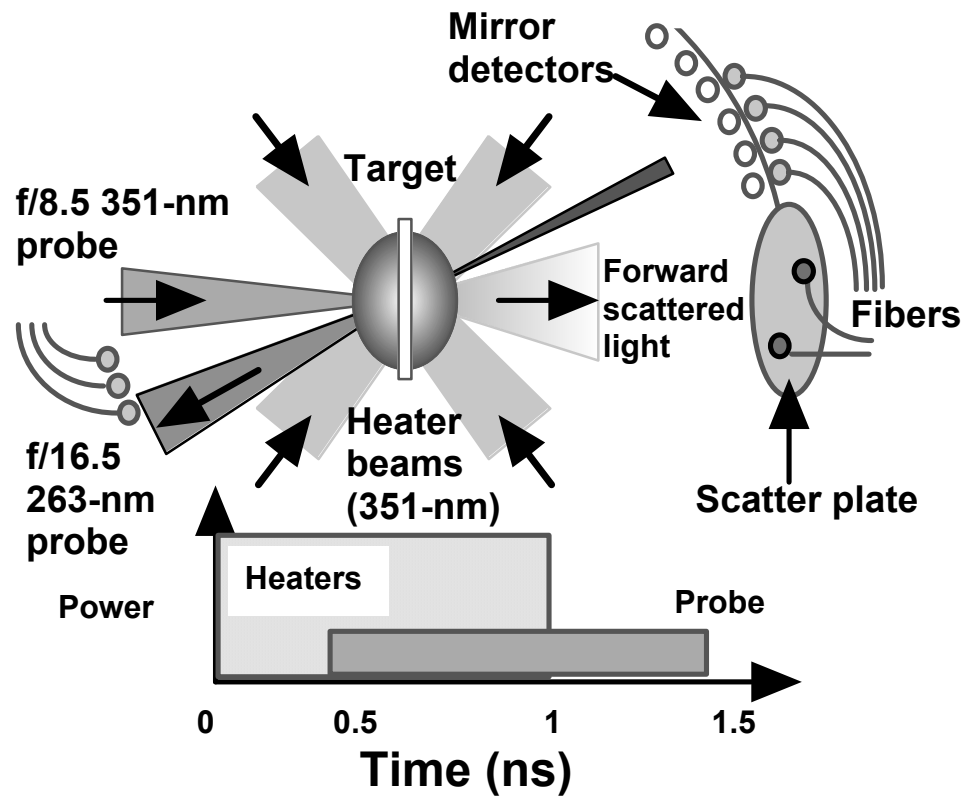


Figure 1 (b)

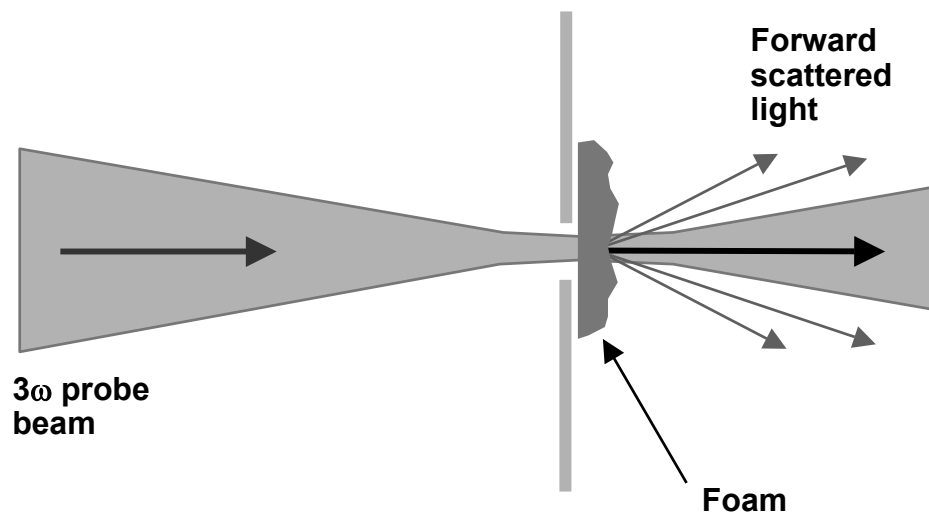


Figure 2 (a)

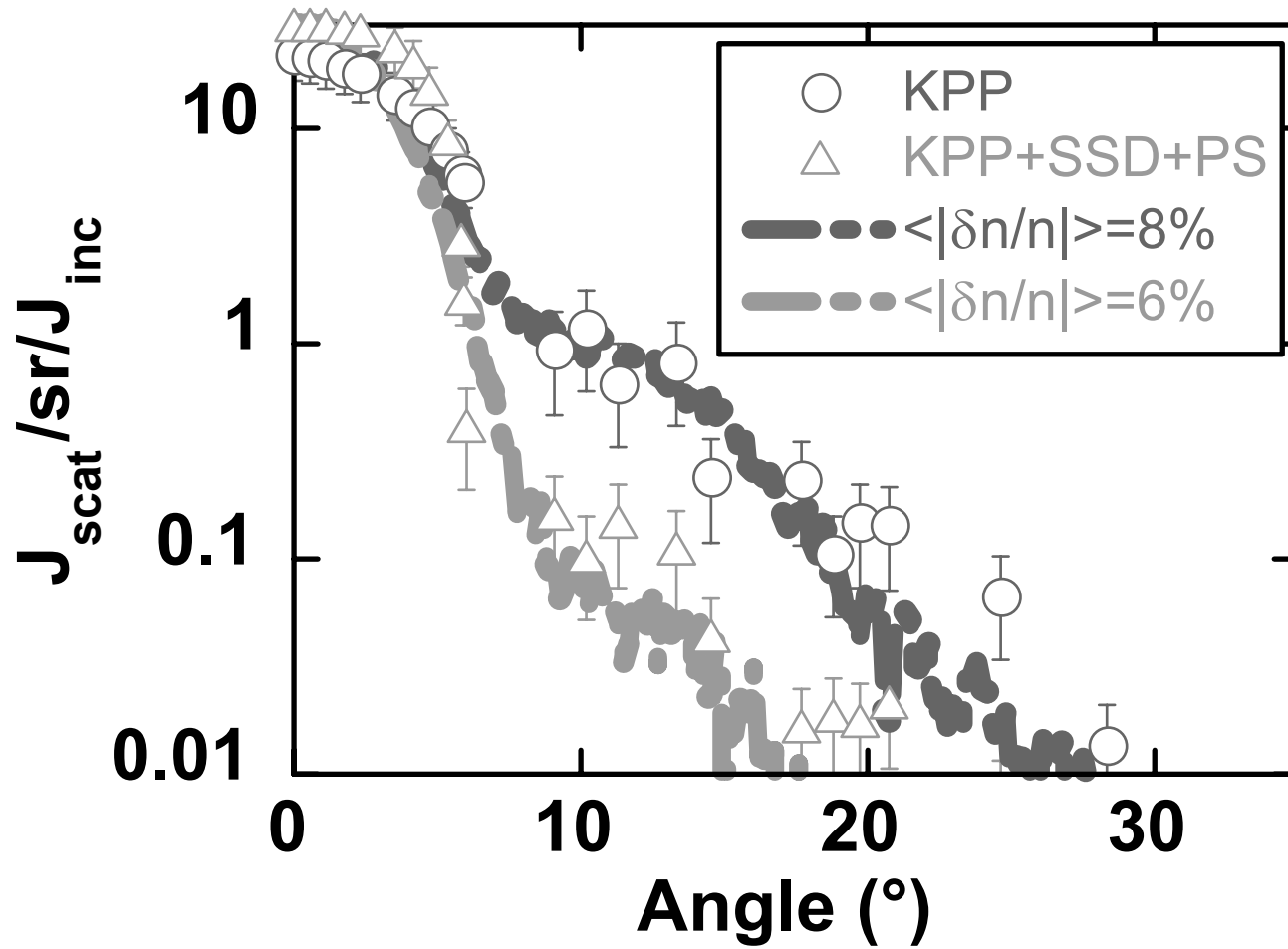


Figure 2 (b)

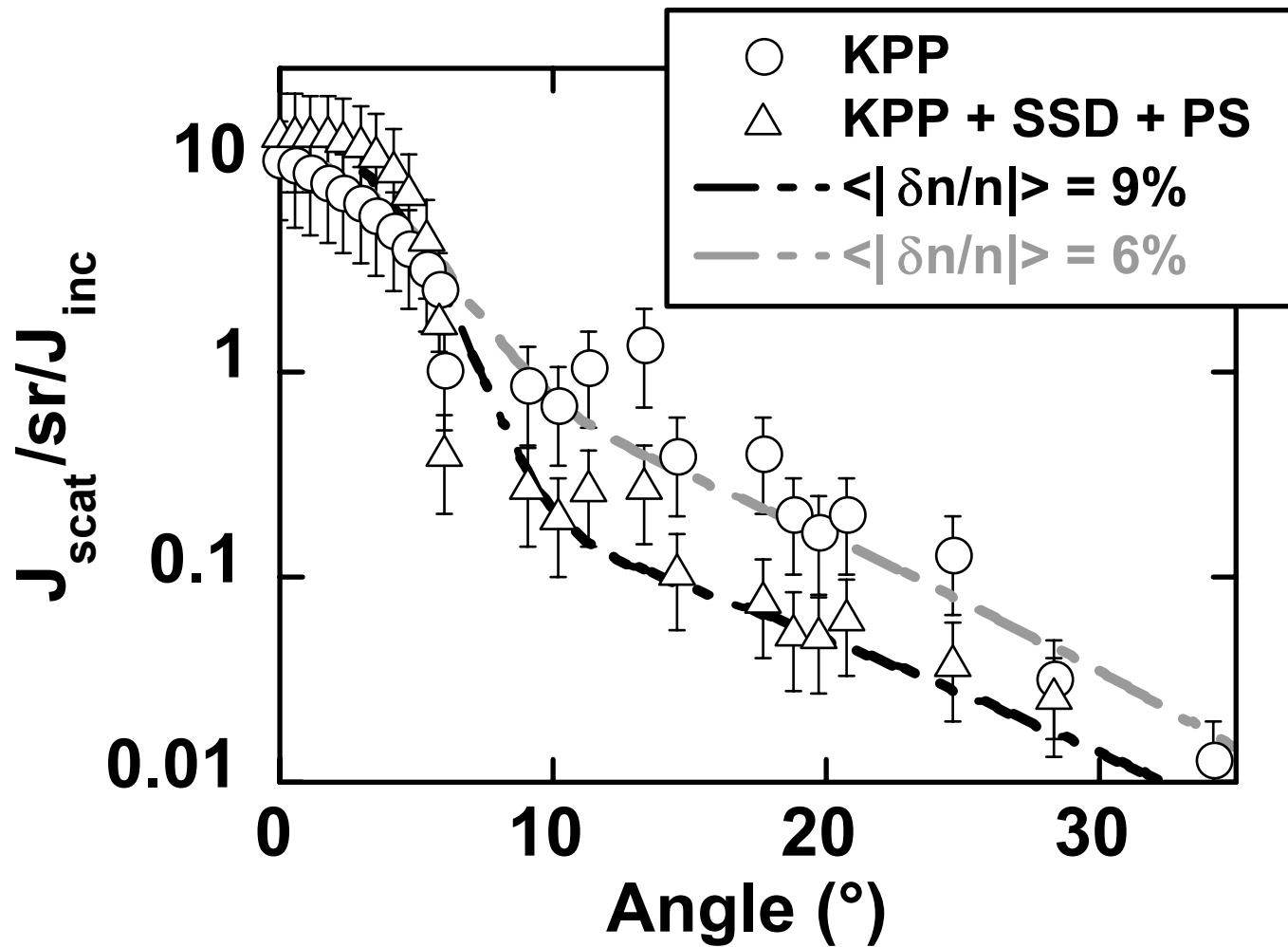


Figure 3

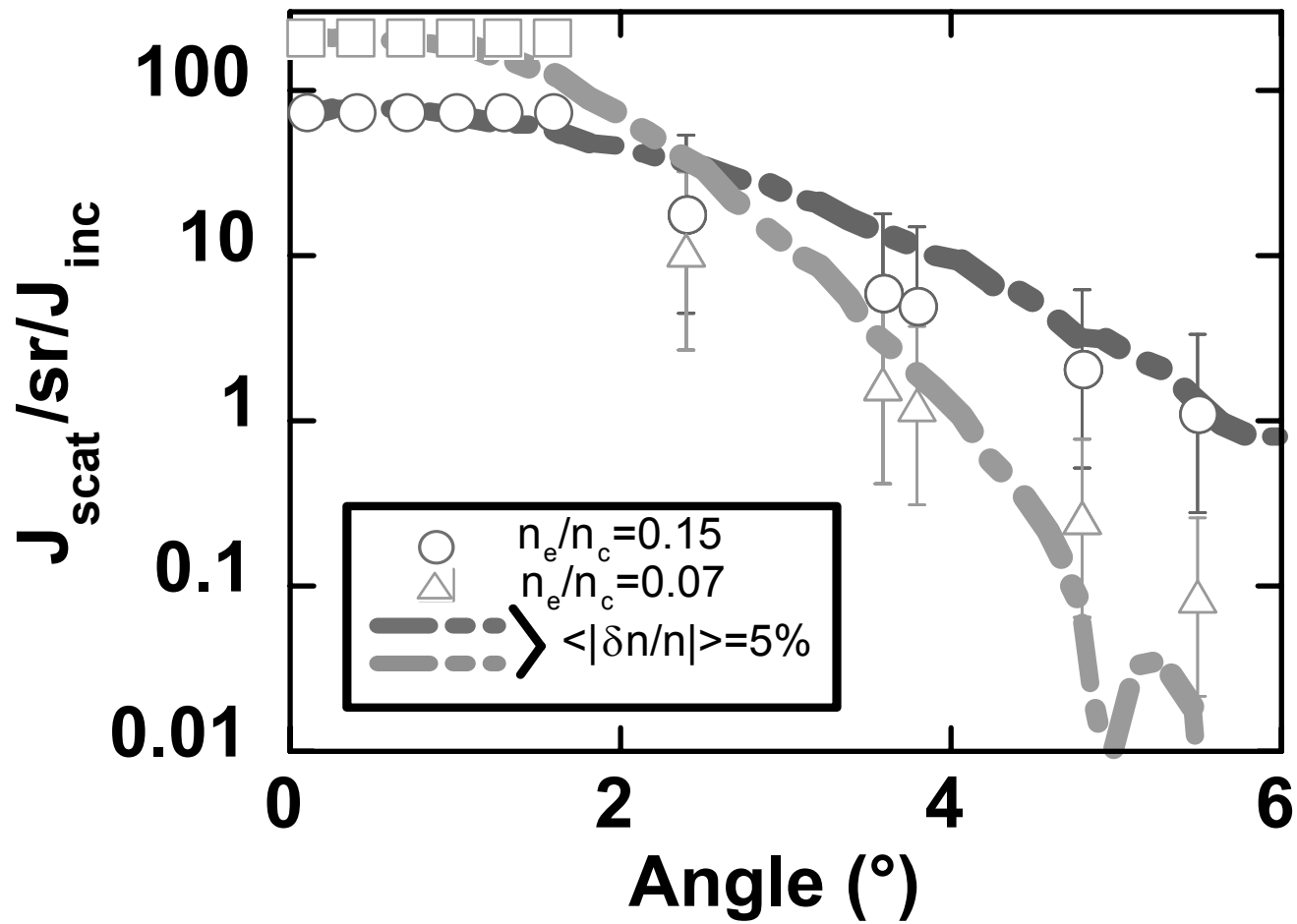


Figure 4

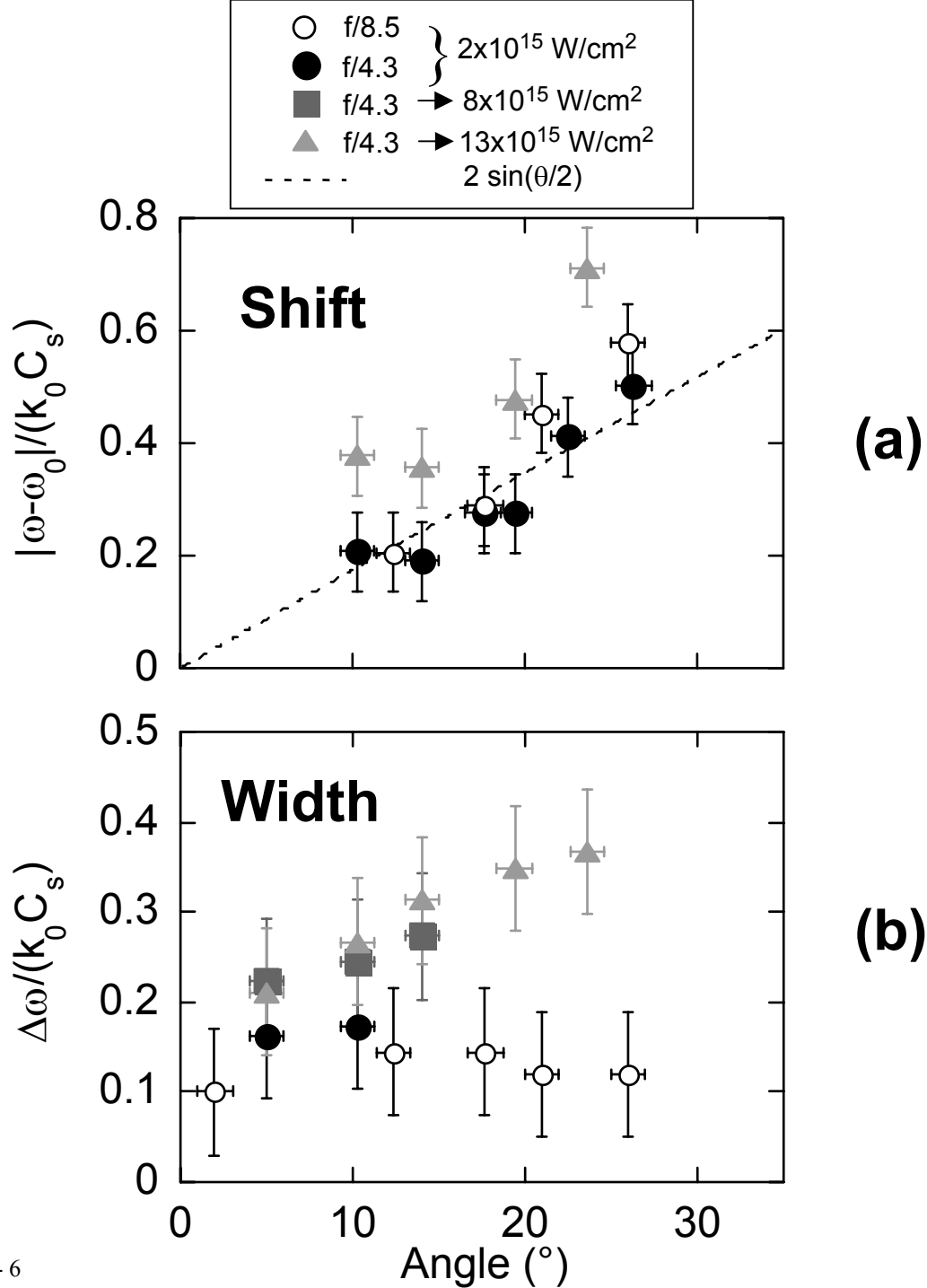


Figure 5

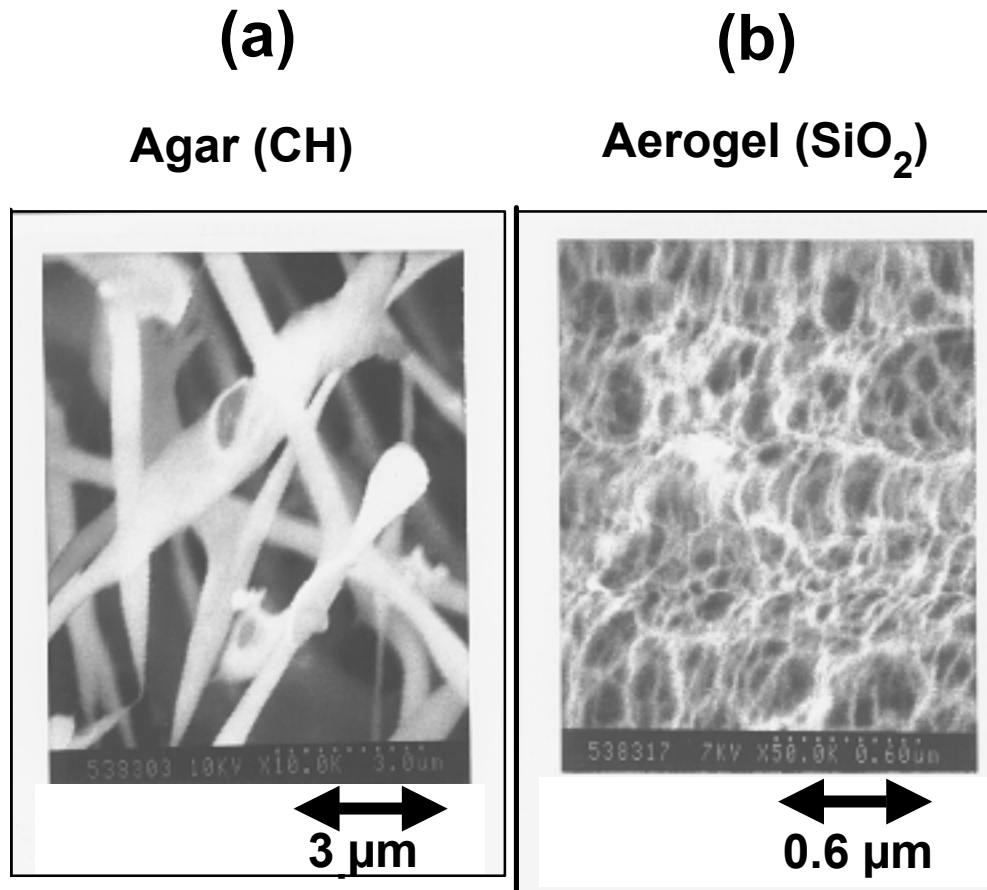


Figure 6

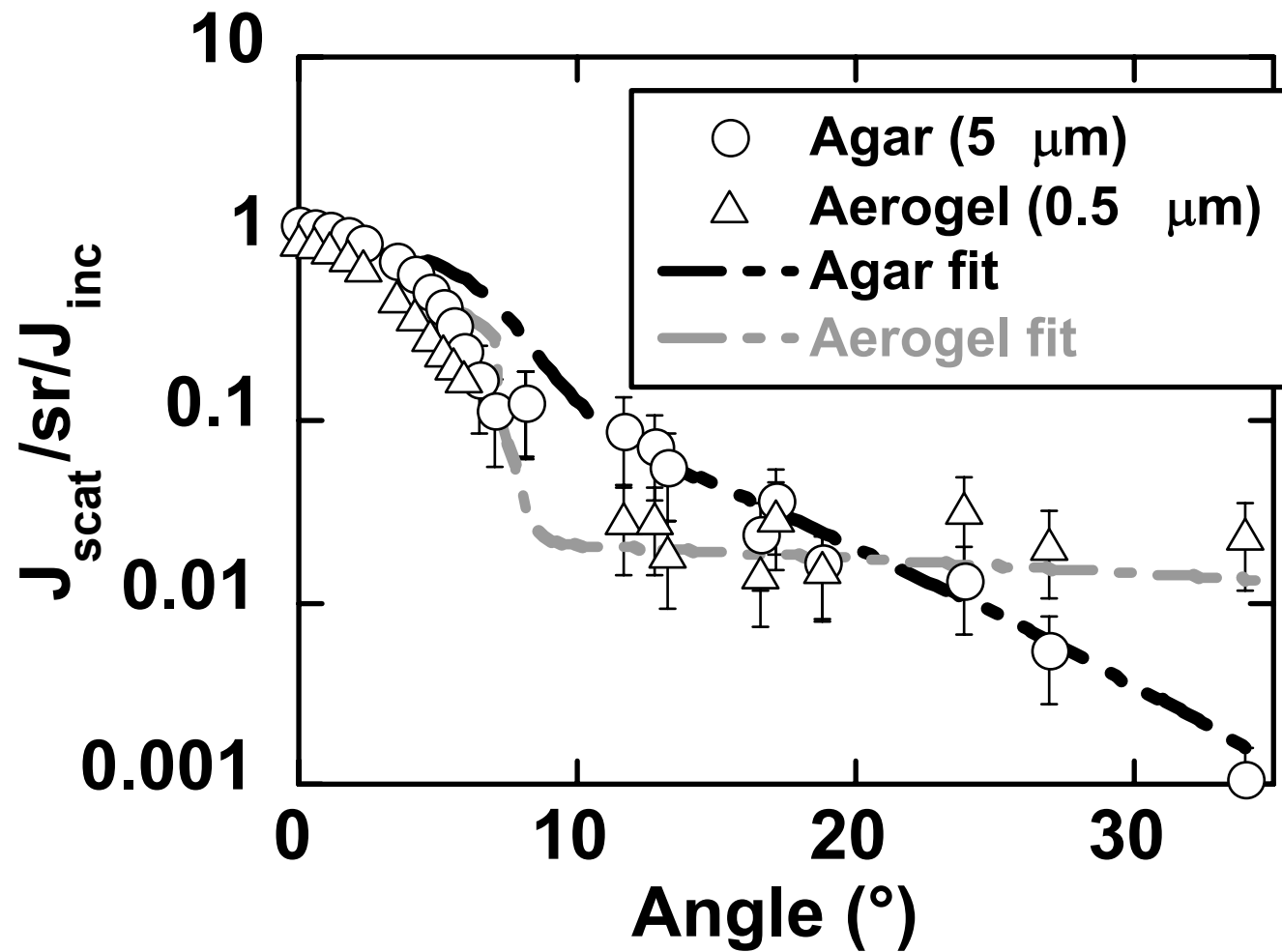


Figure 7 (a)

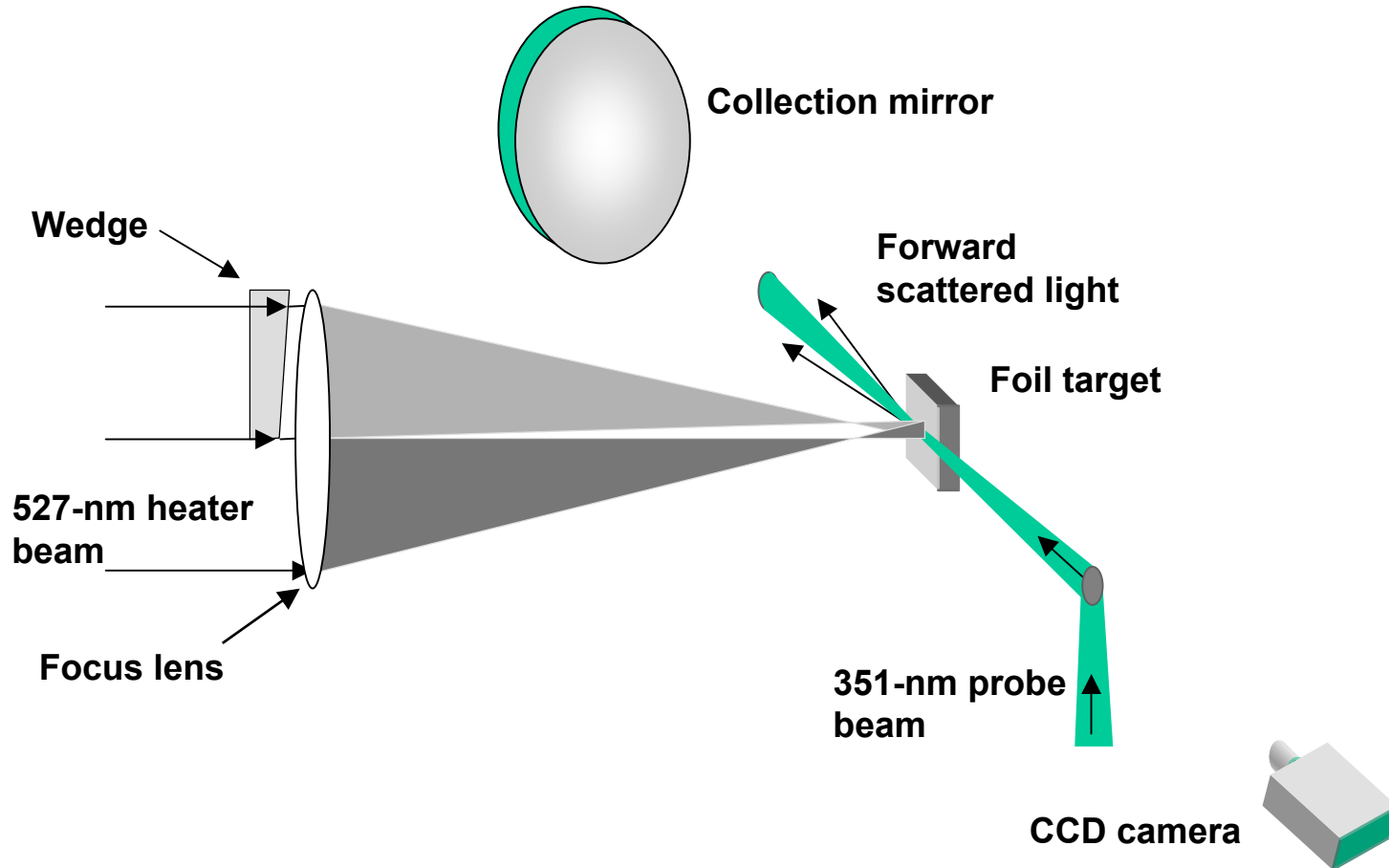


Figure 7 (b)

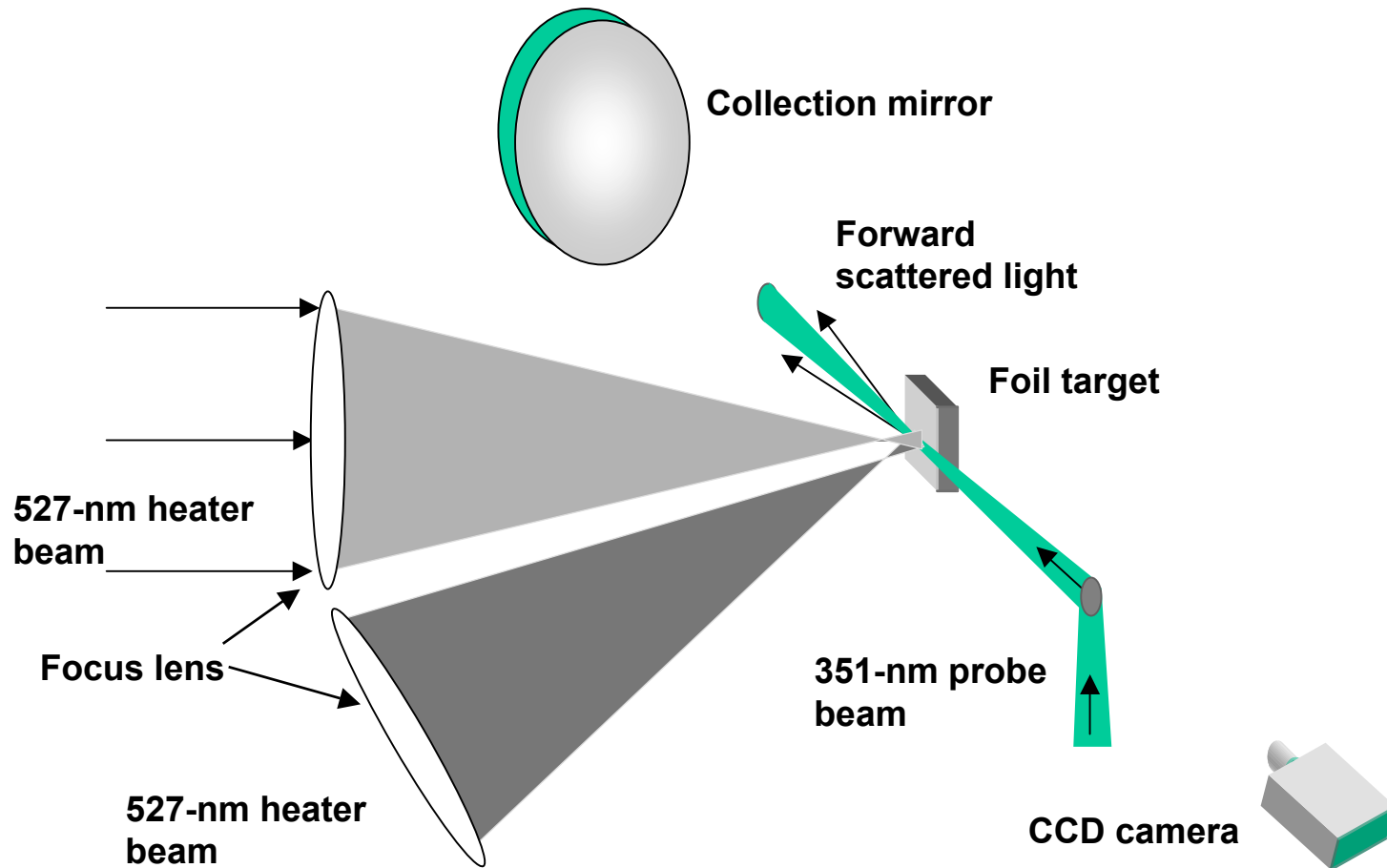


Figure 8 (a)

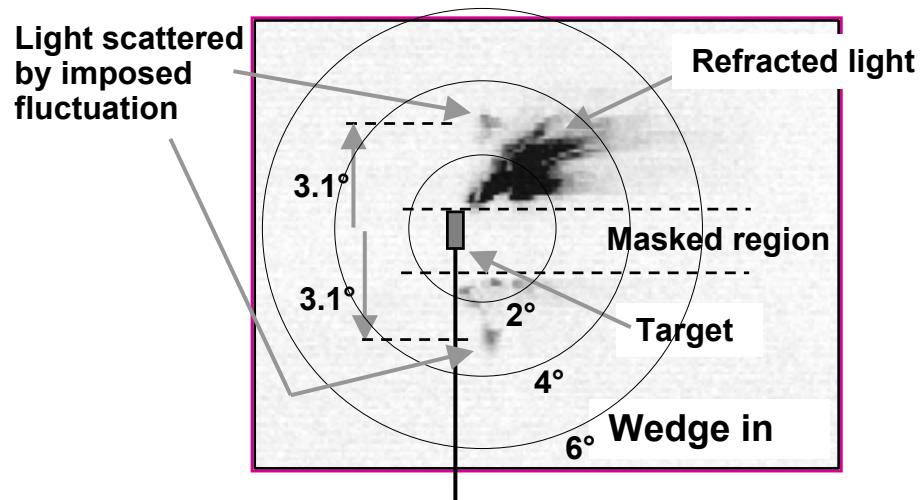


Figure 8 (b)

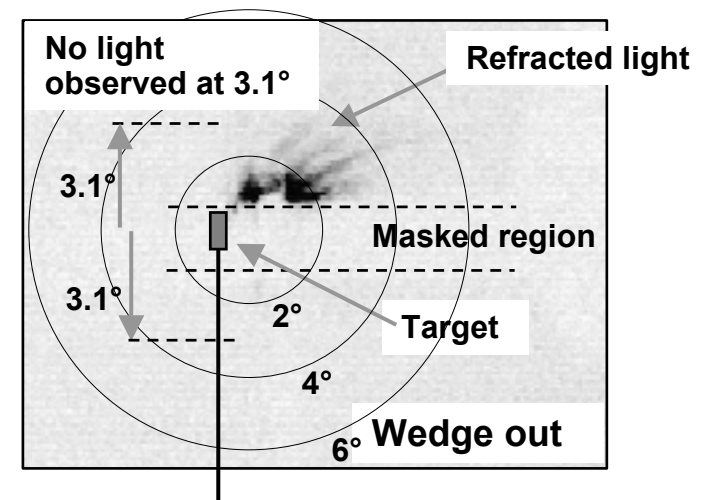


Figure 9

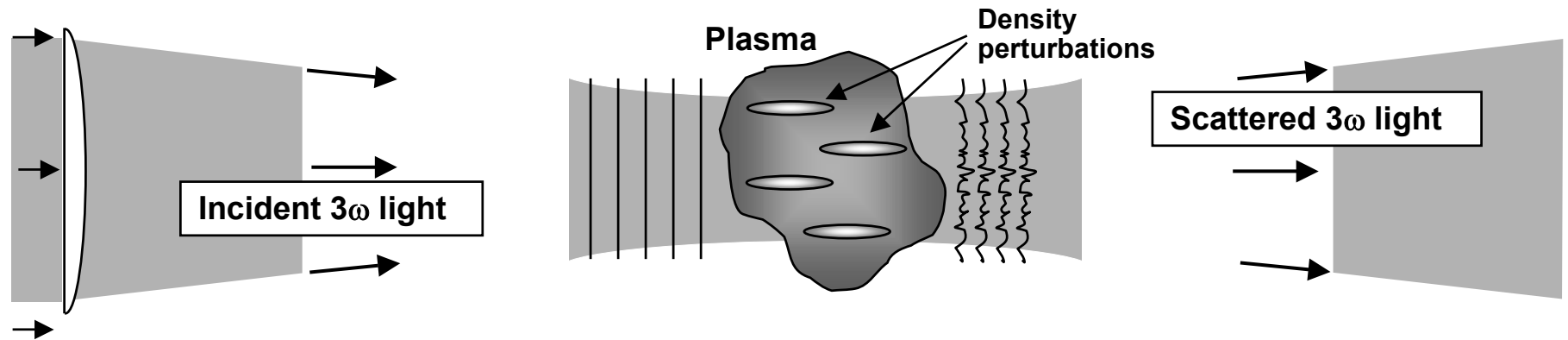


Figure 10 (a)

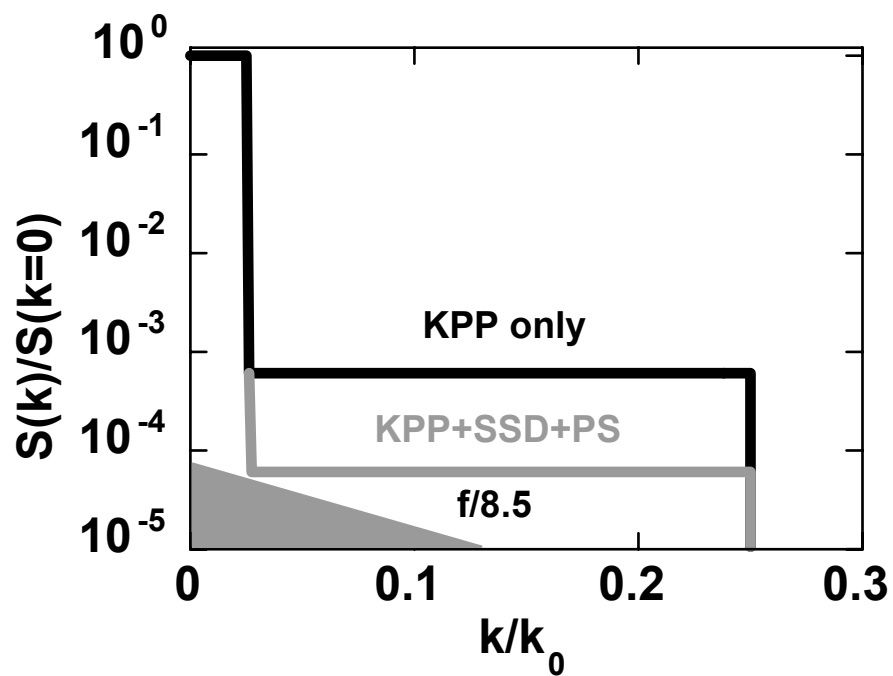


Figure 10 (b)

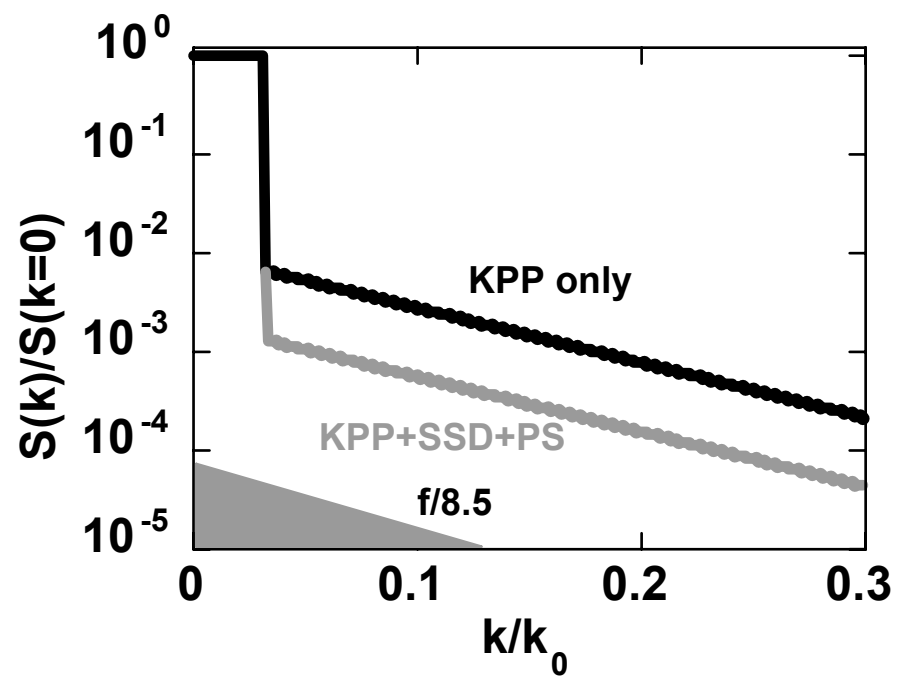


Figure 11

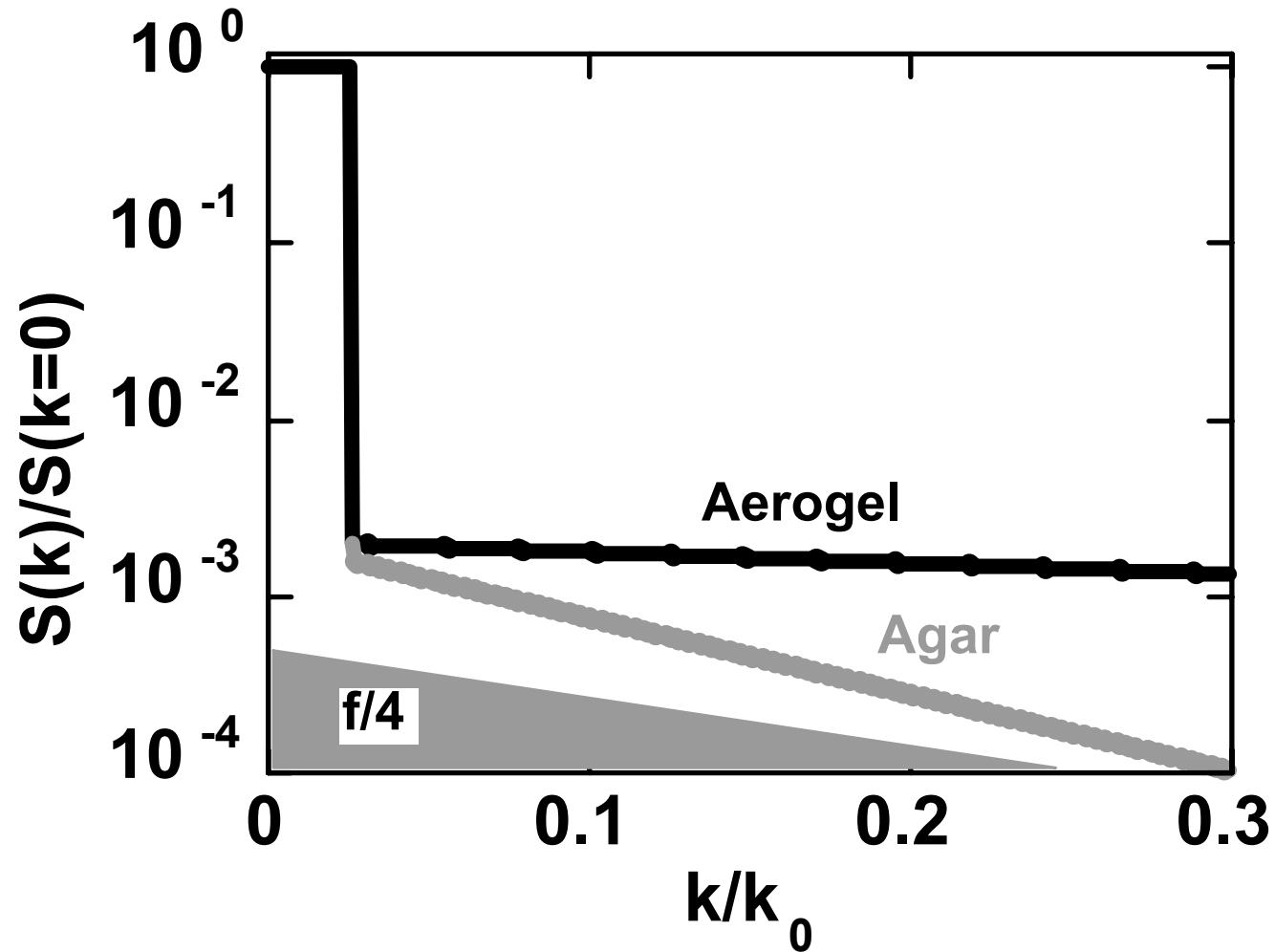


Figure 12 (a)

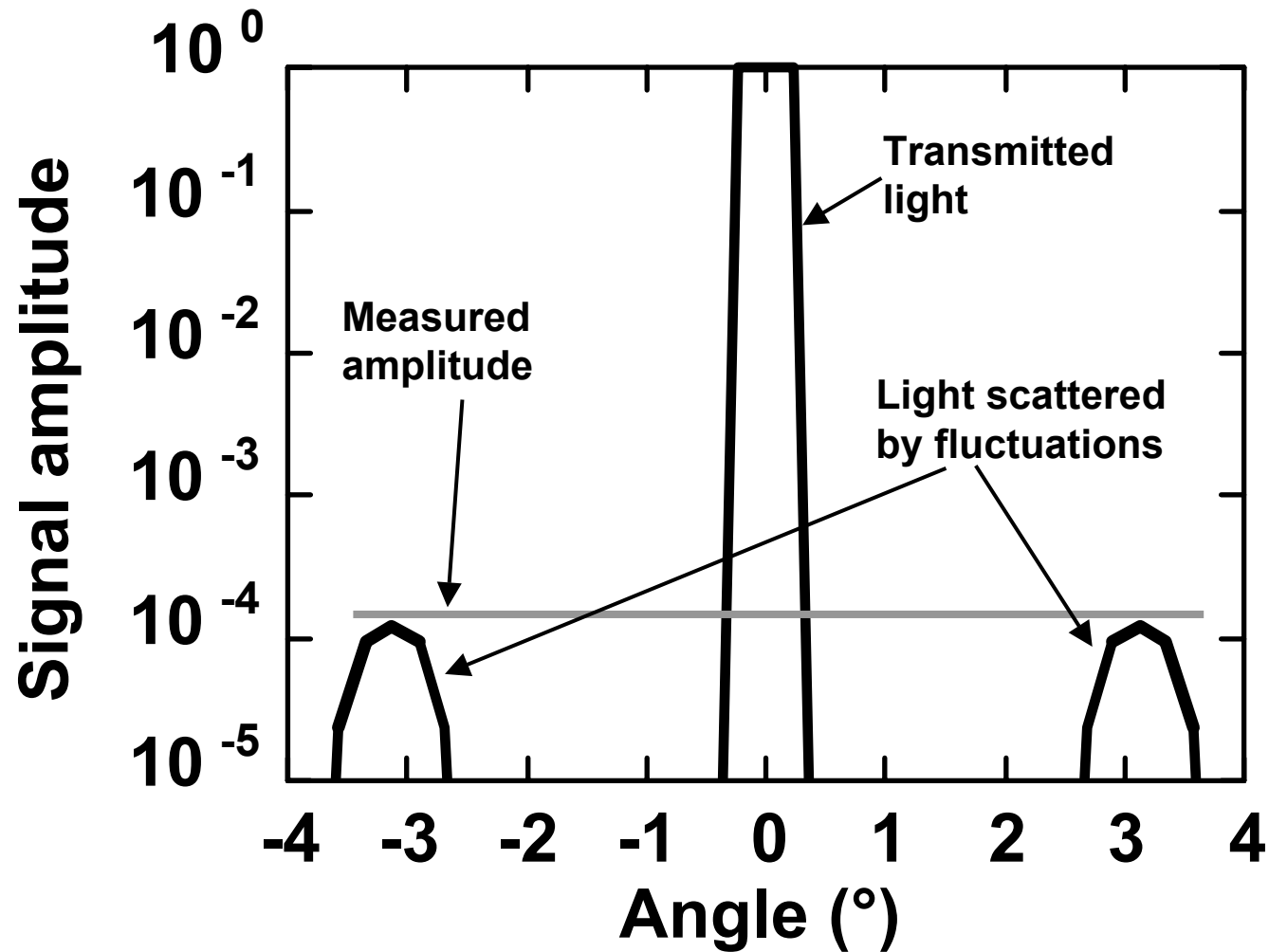


Figure 12 (b)

